

Immersed boundary method for dynamic simulation of polarizable colloids of arbitrary shape in explicit ion electrolytes

Emily Krucker-Velasquez,¹ James W. Swan,¹ and Zachary Sherman²

¹*Department of Chemical Engineering, Massachusetts Institute of Technology, Cambridge, Massachusetts 02139, USA*

²*Department of Chemical Engineering, University of Washington, Seattle, Washington 98195, USA*

(*Electronic mail: zsherm@uw.edu)

(Dated: June 18, 2024)

We develop a computational method for modeling electrostatic interactions of arbitrarily-shaped, polarizable objects on colloidal length scales, including colloids/nanoparticles, polymers, and surfactants, dispersed in explicit ion electrolytes and nonionic solvents. Our method computes the nonuniform polarization charge distribution induced in a colloidal particle by both externally applied electric fields and local electric fields arising from other charged objects in the dispersion. This leads to expressions for electrostatic energies, forces, and torques that enable efficient molecular dynamics and Brownian dynamics simulations of colloidal dispersions in electrolytes, which can be harnessed to accurately predict structural and transport properties. We describe an implementation in which colloidal particles are modeled as rigid composites of small spherical beads that tessellate the surface of the particle. The electrostatics calculations are accelerated using a spectrally-accurate particle-mesh-Ewald technique implemented on a graphics processing unit (GPU) and regularized such that the electrostatic calculations are well-defined even for overlapping bodies. We demonstrate the effectiveness of this approach through a series of calculations, including the induced dipole moments and forces for one, two, and lattices of spherical colloids in an electric field; the induced dipole moment and torque for anisotropic particles in an electric field; the equilibrium distribution of ions in the double layer around charged colloids; the dynamics of charged colloids; and ions in the double layer around a polarizable colloid exposed to an electric field.

I. INTRODUCTION

The equilibrium and dynamic properties of colloidal suspensions are critical for a wide variety of industrial applications. Colloidal suspensions can be as simple as gold particles in water or be present in more sophisticated structures such as micelles, vesicles, nanocapsules, and dendritic polymers to name a few¹ (herein simply colloidal particles). When immersed in a dielectric fluid, colloidal particles often acquire charges. The resulting many-body electrostatic interactions inform the macroscopic properties of the suspension.² For example, charged colloids attract oppositely charged species to the colloid-fluid interface, giving rise to what is commonly referred to as the “electric double layer” (EDL).³ The thickness of this microscopic electric double layer greatly influences the strength of interactions among the colloids and consequently the thermodynamic stability of the suspension.^{2,3} Furthermore, charged colloids and their respective ionic clouds behave as quasiparticles in the presence of phoretic forces; thus, the thickness of the EDL controls the electrophoretic mobility of the particles.³⁻⁵ Alternatively, polarization effects can lead to emergent transport processes. This is the case for polarizable colloidal particles in an external electric field. The field induces a nonuniform surface charge distribution giving rise to the nonlinear electrokinetic phenomenon known as “induced charge electro-osmosis”.⁶

Several continuum theories have been developed to describe these effects, the most common of which are Debye-Huckel theories for equilibrium properties and the “standard model” of electrokinetics for dynamic properties,³ both of

which consider noninteracting point ions. Because these theories ignore ion-ion correlations and excluded volume interactions, they are inaccurate for a range of conditions important in colloidal suspensions, including strongly charged colloids,² concentrated electrolytes, and ionic liquids.⁷

Particle-based simulations can be tailored to include such ion-ion correlations and excluded volume interactions. For example, several molecular dynamics, multiparticle collision dynamics, and Monte Carlo techniques have been developed to model electrostatic interactions in colloidal systems⁸⁻¹³. Nevertheless, the majority of previous computational work considers only pairwise additive Coulombic potentials between charged species and does not consider the importance of three-body and higher-order (many-body) interactions. While useful for certain classes of problems, these simplifications disregard 1) charges that may be induced in polarizable bodies due to global or local electric fields and 2) many-body effects on the energies and forces of these polarizable bodies. These time- and configuration-dependent “induced charge” effects are important for accurately describing the structure of ionic double layers,¹⁴ stability and self-assembly of colloidal suspensions,¹⁵⁻¹⁷ and particle and fluid dynamics in electric fields.⁶

In general, the level of “coarse-graining” strongly influences the level of accuracy of particle-based simulations. There are different levels of coarse-graining that can be used when simulating colloidal suspensions. The highest level of refinement at the length scale of our interest is present in conventional all-atom molecular dynamics. Here, each of the atoms in the suspension is replaced by appropriately scaled beads whose interparticle interactions are approximated via

force fields. All-atom simulations, however, are prohibitively expensive when colloidal systems are studied because of the significant difference between the solvent and colloidal particles' sizes. A single 10^{-8} m colloid comprises approximately 2×10^4 particles.¹⁸ Common solvents, such as water, are on the length scale of 10^{-2} the diameter of this colloidal particle. It would be necessary to simulate a number in the order of 10^6 solvent molecules per unit volume of colloid. Thus, this level of detail hinders our ability to simulate even a small number of colloids. For example, if one considers simulating four colloidal particles in a tetrahedral packing density; this would be equivalent to solving 10^7 equations of motion each time step and keeping track of the equivalent number of positions and velocities.

In contrast, continuum models are highly coarse-grained. Continuum approximations, such as the Poisson-Boltzmann (PB) equation, commonly assume that colloidal particles lie in a solvent of constant permittivity and only experience the *average* behavior of other neighboring charged species. In these models, polarization, many-body effects, and thermal fluctuations can noticeably increase the complexity of the formulation of the problem and preclude analytic progress. Therefore, these effects are often ignored in purely continuum models, and consequently, this simplified representation of charged soft matter systems is only accurate in a finite range of regimes. This range can broaden if thermal fluctuations are explicitly included in the simulation.¹⁹

Within the level of detail present in all-atom simulations and continuum models, there are alternative schemes that allow us to reduce the computational cost of simulating at the colloidal scale. Brownian dynamics (BD), for example, can be used to describe the motion of discrete particles in a continuum Newtonian fluid. This significantly decreases the computational resources needed to track the positions and velocities of the solvent. When coupled with Stoke's equation (known as Stokesian Dynamics)^{20,21} this hybrid method can be used for a wide range of concentrations to numerically extract the dynamic and static properties of assembly particles whose radii range from 10^{-9} m (seen in the average hydrated diameter of sodium chloride in solution) to 10^{-3} m,^{2,22} without the need to explicitly simulate the solvent molecules.

Alternatively, different numerical methods can be used to solve Poisson's equation and compute the interparticle forces in electrostatically stabilized colloidal suspensions. Some of these numerical treatments are finite differences, finite elements, and finite boundary methods. However, this can be a difficult task due to the long-ranged and many-body nature of electrostatic interactions.

These techniques to solve partial differential equations, however, require at least the discretization of the entire 2D space (finite difference and finite element methods discretize the entire 3D space), which is computationally costly. Various numerical schemes and approximations have emerged to overcome this problem. One of the simplest ways to avoid discretization of space is through effective interaction potentials. Particle-based simulations often treat the ions and colloids as discrete particles that interact through some

effective Yukawa-type interaction potential (see, for example, ref.²³ or ref.²⁴). This circumvents the need to otherwise compute the electric potential in the simulation box, but inherits some of the same shortcomings as mean-field theories. Alternatively, if the assumption of spherical particles is valid, then a closed form for Greens' function, in the form of a harmonic sum, can be obtained in some cases.²⁵ Moreover, a closed form solution for Greens' function can sometimes be obtained using the Image Charge Method (ICM) for simple geometries.²⁵⁻²⁷ Other standard methods that do not require the discretization of the simulated volume are the Method of Moments (MoM)^{28,29} and the perturbative many-body expansion method,³⁰ which finds the potential (including polarization) from a scattering expansion. These techniques, however, can be prohibitively expensive if large systems are studied (e.g. ICM scales with the number of particles, N , as $\sim N^3$, for large N) or the particles are too close together (for example, MoM requires a large number of moments to converge in concentrated systems). Hybrid methods have also emerged to simulate spherical particles that scale linearly with the number of particles in the system³¹, but are strictly applicable to colloidal spherical particles. Significant effort has been put into decreasing the computational time required to solve for the induced charge effects in soft matter systems relying on boundary element formulations.³²⁻³⁴ For example, the induced charge has been related to the electric field to obtain a system of equations in the form of $A\mathbf{s} = \mathbf{b}$, where \mathbf{b} depends on the free charge, \mathbf{s} is a vector of discretization points on the surface of interest. A depends on the geometry of the system and can take the form of a linear operator \mathcal{A} ,³² or as weights of a linear combination of nodes, \mathbf{A} .³⁵ The ICC* method, for example, proposes to use the successive over-relaxation method to solve for the charge distribution at a later time step in coarse-grained dynamic simulations, avoiding the need to invert the weighting coefficients matrix each time step.³⁵

When solving for the electrostatic potential, an additional obstacle arises due to the long-range nature of the electrostatic forces, which decay as $O(1/r)$ with the distance from the particle, r . This becomes particularly demanding when periodic boundary conditions are used. In particle-based computer simulations, these are commonly computed using mesh-based variants of the Ewald sum method, which splits the interparticle interactions into short and long range and solves for them in real and Fourier space, respectively.^{34,36,37} For non-periodic systems, the Fast Multipole Method is preferred.^{38,39}

Given the limitations of non-mesh-based methods for simulating systems with a large number of particles and the inability of Poisson-Boltzmann-type treatments to accurately consider packing and polarization effects, it is necessary to develop even faster methods for dynamic simulations of colloidal systems. Here, we apply the immersed boundary method to simulate the electrostatically stabilized colloidal suspensions at the mesolevel. We take advantage of a spectrally accurate Ewald summation type (SE, for spectral Ewald) driven by graphics processing units (GPUs) to accelerate the computation of the electrostatic forces and

polarization due to local and external fields. The SE technique has also been used to calculate long-range interparticle hydrodynamic interactions for dynamic simulations of dense suspensions,^{40,41} and, more recently, for the rapid computation of the stress tensor of mutually polarizable spheres.⁴² The manuscript is organized as follows, Sect. II, brief background on the formulation of electrostatic interactions between spherical particles in a periodic geometry. In Sect. III, we describe the immersed boundary method to calculate electrostatic forces on arbitrarily shaped polarizable bodies. Section IV presents a series of validation calculations for the immersed boundary method. Finally, Sect. V shows its use for Brownian dynamic simulations of electric double layers and the response of an ideally polarizable colloidal particle immersed in an electrolyte to an external electric field. These out-of-equilibrium simulations show the applicability of the method to obtain dynamic properties of colloidal suspensions, such as the electrophoretic velocity of charged colloids as a result of an electric field and the induced charge electro-osmosis phenomenon.⁴³

II. BACKGROUND / GRAND POTENTIAL MATRIX DERIVATION

Electrostatic phenomena in colloidal dispersions are described by Poisson's equation for the electrostatic potential $\psi(\mathbf{x})$

$$\nabla \cdot \mathbf{E} = \frac{\rho}{\varepsilon}, \quad \mathbf{E} = -\nabla\psi \quad (1)$$

where $\mathbf{E}(\mathbf{x})$ is the electric field, $\rho(\mathbf{x})$ is the free charge density and $\varepsilon(\mathbf{x})$ is the electric permittivity. The free charge is localized to colloids and ions so that $\rho(\mathbf{x}) = 0$ everywhere for \mathbf{x} in the fluid. These assumptions reduce Poisson's equation to the simpler Laplace equation with boundary conditions on the surfaces,

$$\nabla^2\psi = 0, \quad (2)$$

$$\psi_p = \psi_f, \quad (\varepsilon_f \mathbf{E}_f - \varepsilon_p \mathbf{E}_p) \cdot \hat{\mathbf{n}} = q_\alpha / (4\pi a^2), \quad (3)$$

where ψ_p and ψ_f are the potentials inside and outside the particle, $q_\alpha / (4\pi a^2)$ is the uniform free surface charge density of ion α on a spherical shell with radius a and net charge q_α , $\hat{\mathbf{n}}$ is the normal outward vector and \mathbf{E}_f and \mathbf{E}_p are the electric field outside and inside the particle, respectively.^{44,45} Further, there may be an externally applied electric field and potential $\mathbf{E}_0 = \nabla\psi_0$, where $\psi(\mathbf{x}) = \psi_0$ in the absence of particles, and we require triply periodic boundary conditions. The time scale of particle motion, $O(1 \mu\text{m}-1 \text{s})$, is orders of magnitude greater than the electric and magnetic relaxation times at the atomic level, $O(10^{-9} \text{s})$, the electric potential $\psi(\mathbf{x})$ is pseudo-steady, and time dependence emerges solely through the time-varying boundary conditions in (3). For a point \mathbf{x} in the fluid,

the potential is given by the integral form of Laplace's equation;

$$\psi_f(\mathbf{x}) - \psi_0(\mathbf{x}) = \frac{1}{\varepsilon_f} \sum_\alpha \int_{S_\alpha} d\mathbf{x}' \left(G(\mathbf{x} - \mathbf{x}') \mathbf{E}_f(\mathbf{x}') \cdot \hat{\mathbf{n}}_{\mathbf{x}'} \right. \\ \left. + \varepsilon_f \psi_f(\mathbf{x}') \hat{\mathbf{n}}_{\mathbf{x}'} \cdot \nabla_{\mathbf{x}'} G(\mathbf{x} - \mathbf{x}') \right), \quad (4)$$

where G is Green's function for Laplace's equation. We can enforce periodic boundary conditions on ψ at this stage by using the periodic Green's function satisfying $-\nabla^2 G(\mathbf{x}) = \sum_{\mathbf{n}} \delta(\mathbf{x} - \mathbf{n})$ where $\mathbf{n} = [n_x L_x, n_y L_y, n_z L_z]$, n_i are integers, and L_i are the periodicities in each dimension. This periodic Green's function admits a spherical harmonic expansion;

$$G(\mathbf{x} - \mathbf{y}) = \frac{1}{V} \sum_{\mathbf{k} \neq 0} \frac{e^{i\mathbf{k} \cdot \mathbf{x}}}{k^2} = \frac{1}{V} \sum_{\mathbf{k} \neq 0} \frac{e^{i\mathbf{k} \cdot (\mathbf{x} - \mathbf{x}_j)}}{k^2} \sum_\ell \sqrt{4\pi(2\ell + 1)} i^{-\ell} \\ \times j_\ell(ka) \left(\frac{r}{a}\right)^\ell Y_\ell(\theta, \phi), \quad (5)$$

which allows (4) to be written in terms of multipole moments,

$$\psi_f(\mathbf{x}) - \psi_0(\mathbf{x}) = \frac{\varepsilon_f}{V} \sum_{\mathbf{k} \neq 0} \sum_\alpha \frac{e^{i\mathbf{k} \cdot (\mathbf{x} - \mathbf{x}_\alpha)}}{k^2} \left(q_\alpha j_0(ka) - \frac{3i}{a} j_1(ka) \mathbf{S}_\alpha \cdot \hat{\mathbf{k}} \dots \right), \quad (6)$$

where $j_i(x)$ is the spherical Bessel function of the first kind of i^{th} order, $\mathbf{k} = [2\pi\kappa_x/L_x, 2\pi\kappa_y/L_y, 2\pi\kappa_z/L_z]$ for integers κ_i , and $\hat{\mathbf{k}}$ the unit vector in the \mathbf{k} direction. The $j_i(ka)$ terms are called "shape factors" that account for how spherical particles propagate electric potentials through Fourier space. Note that due to periodic boundary conditions, equation (4) should also contain a contribution from an integral over a closed surface at infinity (S_∞). Bonnecaze and Brady show⁴⁶ that including this S_∞ integral is equivalent to enforcing electroneutrality by removing the $\mathbf{k} = 0$ term, so we will not consider it here.⁴⁷ Integrating on the surface of each particle, applying the boundary conditions in (3), and retaining only the first moment of expansion,

$$\psi_\alpha(\mathbf{x}_\alpha) - \psi_0(\mathbf{x}_\alpha) = \frac{\varepsilon_f}{V} \sum_{\mathbf{k} \neq 0} \sum_\beta j_0^2(ka) \frac{e^{i\mathbf{k} \cdot (\mathbf{x}_\alpha - \mathbf{x}_\beta)}}{k^2} q_\beta. \quad (7)$$

where $\psi_\alpha = \frac{1}{4\pi a^2} \int_{S_\alpha} d\mathbf{x} \psi_p(\mathbf{x})$ is the surface average ψ_p of the particle α . Note that the β sum includes the $\beta = \alpha$ term, i.e. the self-term, is naturally incorporated into (9). Higher-order moments can be retained in (9),⁴⁷ e.g. to account for dipole-dipole interactions among particles,¹⁵ but here we consider only charges. Equation (9) is a system of equations that relates each of the N particle potentials ψ_α to the N particle charges q_β , which we represent in matrix-vector form,

$$\Psi - \Psi_0 = \mathcal{M}^E \cdot \Omega, \quad (8)$$

where $\Psi - \Psi_0 = [\psi_1 - \psi_0(\mathbf{x}_1), \psi_2 - \psi_0(\mathbf{x}_2), \dots, \psi_N - \psi_0(\mathbf{x}_N)]^T$ is a list of particle potentials relative to the external

potential at their centers, $\mathcal{Q} = [q_1, q_2, \dots, q_N]^T$ is the list of particle charges, and \mathcal{M}^E is named the potential tensor, with elements

$$M_{\alpha\beta} = \frac{\epsilon_f}{V} \sum_{\mathbf{k} \neq 0} j_0^2(ka) \frac{e^{i\mathbf{k} \cdot (\mathbf{x}_\alpha - \mathbf{x}_\beta)}}{k^2}. \quad (9)$$

In real space, these elements are

$$M_{\alpha\beta} = \begin{cases} \frac{1}{4\pi a \epsilon_f r}, & r \geq 2a \\ \frac{4a - r}{16\pi a \epsilon_f}, & r < 2a \end{cases} \quad (10)$$

$M_{\alpha\beta}$ is identical to the Coulomb interaction when the particles do not overlap ($r \geq 2a$). For overlapping particles ($r < 2a$), $M_{\alpha\beta}$ regularizes this Coulomb interaction. Though overlaps do not correspond to any physically-realizable configuration, they often occur in many kinds of molecular simulations. It is impossible to satisfy the boundary conditions (3) for overlapping particles, so the choice of regularization is arbitrary. The particular form of $M_{\alpha\beta}$ here is advantageous because (1) it ensures that \mathcal{M}^E is always positive definite, (2) it ensures that \mathcal{M}^E is well-conditioned, as no elements diverge, and (3) it decays more quickly ($\sim 1/k^4$) than normal Coulomb interactions ($\sim 1/k^2$). As we explain in Section III D, these features enable efficient numerical calculations to compute electrostatic forces.

III. IMMERSSED BOUNDARY METHOD FOR ELECTRIC FORCES OF ARBITRARILY SHAPED CONDUCTORS

Immersed boundary (IB) methods for solving partial differential equations provide a faster alternative to standard body-conforming gridding methods for dealing with moving boundaries and interfaces with complex geometries. In general, immersed boundaries require two independent discretizations: one discretization for the body surfaces and a second for the fluid volume.

IB methods have been useful for simulating fluid flow and hydrodynamic interactions in colloidal dispersions,²² electrohydrodynamics⁴⁸ and flow near elastic boundaries⁴⁹. Here, we derive an immersed boundary method for colloidal particles of *arbitrary shape and charge*. The method facilitates the computation of induced polarization on the surface of complex geometries due to local (by other charged bodies) and external fields.

A. Composite Bead Model

In general, we propose to represent the bodies with a composite-bead structure where beads tessellate the bodies' surfaces. Although these beads can take any size, it is convenient to use a single geometric length scale. In our particle-based simulations, the natural and shortest geometric length scale is given by the ion's diameter. Thus, we constrain the tessellating beads to the same diameter in value $2a$.

Simple spherical bodies can be constructed iteratively by placing 12 beads on the vertices of an icosahedron. Then, we can bisect the edges with more beads; projecting the new beads radially outward such that their centers lie on the body surface. This procedure can be repeated until a user-defined discretization level is reached.⁵⁰ This process builds a series of "icospheres" that provide increasing resolution of the body surface as the number of composing beads increases. We have previously found that setting the beads to be as large as possible without overlapping yields a good approximation of the true surface.²² This approach is a type of "immersed boundary method" because we use different, incommensurate discretizations of the body surfaces and the fluid. Surfaces are discretized with the bead tessellation and, consequently, are "immersed" in the Fourier grid that discretizes the fluid.⁴⁷ The error introduced by the level of refinement is tested in sec. IV.

B. Induced Surface Charge Distribution of Polarizable Bodies

Consider a suspension with N_b bodies, where the center of mass of the i^{th} body is \mathbf{X}_i . The surface of each body is made up of N_i beads of radius a at positions \mathbf{x}_{ij} . Ionic species can be considered to be bodies with one constituent particle. Note that we use lowercase variables to indicate individual bead quantities and uppercase variables to indicate rigid body quantities. Lowercase bead quantities with two indices (ij) indicate the j^{th} bead on the i^{th} body, while a single index (β) implies a global bead index (*i.e.* $\beta = (i-1)N_i + j$). The net charge on the i^{th} body is equal to the sum of its constituent bead charges q_{ij} ,

$$Q_i = \sum_j q_{ij}. \quad (11)$$

Here, we assume that bodies are ideally polarizable (*i.e.* $\epsilon_p \rightarrow \infty$), so that the electric potential everywhere in the body is constant and that each bead's potential $\psi_{ij}(\mathbf{x}_{ij})$ is equal to the body's potential $\Psi_i(\mathbf{X}_i)$ to which it belongs, $\psi_{ij} = \Psi_i$.

Bodies with finite ϵ_p have a more sophisticated relation between bead potential and body potential³² and are the subject of future study. The suspension is immersed in a constant electric field, \mathbf{E}_0 , which establishes the external potential $\psi_0(\mathbf{x}) = -\mathbf{x} \cdot \mathbf{E}_0$. The difference between the bead potential and the external potential is

$$\psi_{ij} - \psi_{0,ij} = \Psi_i - \Psi_{0,i} + \mathbf{r}_{ij} \cdot \mathbf{E}_0, \quad (12)$$

where $\mathbf{r}_{ij} \equiv \mathbf{x}_{ij} - \mathbf{X}_i$ is the position of the bead relative to the center of mass of the body. The bead potentials ϕ_α are also related to the body charges q_β through the potential tensor \mathbf{M} in (7).

Typically, the body charges Q_i and the external field \mathbf{E}_0 are known, while the induced bead charges q_α and the body potentials Ψ_i are unknown. We can construct a system of equations for these unknowns by combining equations (7), (11),

and (12)

$$\begin{bmatrix} -\mathbf{M} & \boldsymbol{\Sigma}^T \\ \boldsymbol{\Sigma} & 0 \end{bmatrix} \cdot \begin{bmatrix} \mathbf{q} \\ \boldsymbol{\Psi} - \boldsymbol{\Psi}^0 \end{bmatrix} = \begin{bmatrix} -\mathbf{r} \cdot \mathbf{E}^0 \\ \mathbf{Q} \end{bmatrix}. \quad (13)$$

$\mathbf{q} \equiv [q_{11}, q_{12}, \dots, q_{21}, q_{22}, \dots]^T$ is a list of all N bead charges, $\mathbf{Q} \equiv [Q_1, Q_2, \dots]^T$ is a list of all N_b body charges, $\boldsymbol{\Psi} - \boldsymbol{\Psi}^0 \equiv [\Psi_1 - \Psi_{0,1}, \Psi_2 - \Psi_{0,2}, \dots]^T$ is a list of the difference between the N_b body potentials and the external potential, and $\mathbf{r} \cdot \mathbf{E}_0 \equiv [\mathbf{r}_{11} \cdot \mathbf{E}_0, \mathbf{r}_{12} \cdot \mathbf{E}_0, \dots, \mathbf{r}_{21} \cdot \mathbf{E}_0, \mathbf{r}_{22} \cdot \mathbf{E}_0, \dots]^T$ is a list of N relative bead positions dotted with the external field. $\boldsymbol{\Sigma}$ is an $N_b \times N$ summation tensor whose rows correspond to bodies and columns correspond to beads. Each row is entirely 0, except for N_i consecutive 1 values in the columns corresponding to the N_i beads of the i^{th} body. Further details for constructing $\boldsymbol{\Sigma}$ and subsequent summation tensors are found in the Appendix. Eq. 13 can be solved iteratively⁵¹ for the bead charges of and the rigid body potentials.

The induced dipole moment of a rigid body can then be computed from the bead charges

$$\mathbf{S}_i = \sum_j \mathbf{r}_{ij} q_{ij}. \quad (14)$$

Note that for single-bead bodies $\mathbf{r}_{ij} = 0$. The set of all rigid body moments (charges and dipoles) is then given by

$$\begin{bmatrix} \mathbf{Q} \\ \mathbf{S} \end{bmatrix} = \boldsymbol{\Sigma}' \cdot \mathbf{M}^{-1} \cdot \boldsymbol{\Sigma}'^T \cdot \begin{bmatrix} \boldsymbol{\Psi} - \boldsymbol{\Psi}^0 \\ \mathbf{E}_0 \end{bmatrix}. \quad (15)$$

where $\boldsymbol{\Sigma}'$ is an $4N_b \times N$ summation tensor, whose first N_b rows are identical to $\boldsymbol{\Sigma}$ and whose next $3N_b$ rows look structurally like $\boldsymbol{\Sigma}$ but with each 1 value replaced with \mathbf{r}_{ij} (see Appendix). The quantity $\mathbf{C} = \boldsymbol{\Sigma}' \cdot \mathbf{M}^{-1} \boldsymbol{\Sigma}'^T$ is called the ‘‘grand capacitance tensor’’ of the dispersion and will be referenced in sec. IV C.

C. Forces and Torques

The potential energy of the suspension is expressed as the sum of products of rigid body moments and potential derivatives⁴⁴

$$\begin{aligned} U &= \frac{1}{2} \sum_i (Q_i \Psi_i - \mathbf{S}_i \cdot \mathbf{E}_0) \\ &= \frac{1}{2} \mathbf{Q} \cdot (\langle \boldsymbol{\Psi} \rangle - \boldsymbol{\Psi}^0) \\ &= \frac{1}{2} \mathbf{Q} \cdot \boldsymbol{\Psi}^0 + \frac{1}{2} [\mathbf{q} \quad \langle \boldsymbol{\Psi} \rangle - \boldsymbol{\Psi}^0] \cdot \begin{bmatrix} -\mathbf{r} \cdot \mathbf{E}_0 \\ \mathbf{Q} \end{bmatrix}. \end{aligned} \quad (16)$$

Moreover, the force on each bead is the negative derivative of U with respect to the bead position \mathbf{x}_α , given all other beads remain fixed, $\mathbf{f}_\alpha = -\nabla_{\mathbf{x}_\alpha} U$. Using (13) in (16) and taking the gradient (see Appendix), the force on bead α is

$$\mathbf{f}_\alpha = q_\alpha \mathbf{E}_0 - \frac{1}{2} (\nabla_{\mathbf{x}_\alpha} \mathbf{M}) : \mathbf{q} \mathbf{q} \quad (17)$$

From the distribution of bead forces, we can compute the i^{th} body’s force, \mathbf{F}_i and torque \mathbf{L}_i

$$\mathbf{F}_i = \sum_j \mathbf{f}_{ij}, \quad \mathbf{L}_i = \sum_j \mathbf{r}_{ij} \times \mathbf{f}_{ij}. \quad (18)$$

These forces and torques serve as the input to a rigid body hydrodynamic integrator⁵⁰ that computes the rigid body velocities and angular velocities of the composites.

D. Spectrally-accurate Ewald summation

The speed at which we can iteratively solve (13) is limited by the speed at which we compute the potential-dipole sums in (7). Here we use a particularly efficient, spectrally accurate Ewald summation effort from ref. 52 which we adapt for our regularized form of the Coulombic interaction (9) following ref.⁵⁰. The sum in (7) is split into two rapidly convergent sums

$$\begin{aligned} \langle \Psi \rangle_\alpha - \psi_0(\mathbf{x}_\alpha) &= \frac{\varepsilon_f}{V} \sum_{\mathbf{k} \neq 0} \sum_{\beta} \frac{e^{i\mathbf{k} \cdot (\mathbf{x}_\alpha - \mathbf{x}_\beta)}}{k^2} h(k) j_0^2(ka) \cdot q_\beta \quad (19) \\ &+ \varepsilon_f \sum_{\mathbf{n}} \sum_{\beta} \mathcal{F}^{-1} \left\{ \frac{e^{i\mathbf{k} \cdot (\mathbf{x}_\alpha - \mathbf{x}_\beta)}}{k^2} (1 - h(k)) j_0^2(ka) \right\} \cdot q_\beta, \end{aligned}$$

where $h(k) \equiv \exp(-k^2/4\xi^2)$, ξ is the Ewald splitting parameter controlling the convergence rate of each sum, and \mathcal{F}^{-1} is the inverse Fourier transform.

1. Real-space sum

The real-space contribution to (19) can be computed by explicitly performing the inverse Fourier transform and then directly summing,

$$\begin{aligned} \langle \psi \rangle_\alpha^r - \psi_0^r(\mathbf{x}_\alpha) &= \frac{1}{\epsilon_f} \sum_\beta q_\beta \left(-\frac{r+2a}{32\pi^{3/2}a^2\xi r} e^{-(r_{\alpha\beta}+2a)^2\xi^2} - \frac{r-2a}{32\pi^{3/2}a^2\xi r} e^{-(r_{\alpha\beta}-2a)^2\xi^2} + \frac{1}{16\pi^{3/2}a^2\xi} e^{-r_{\alpha\beta}^2\xi^2} \right. \\ &+ \frac{2\xi^2(r+2a)^2+1}{64\pi a^2\xi^2 r} \operatorname{erfc}(r_{\alpha\beta}+2a)\xi + \frac{2\xi^2(r-2a)^2+1}{64\pi a^2\xi^2 r} \operatorname{erfc}(r_{\alpha\beta}-2a)\xi \\ &\left. - \frac{2\xi^2 r^2+1}{32\pi a^2\xi^2 r} \operatorname{erfc} r_{\alpha\beta}\xi - \left(\frac{1}{4\pi r} + \frac{4a-r}{16\pi a^2} \right) \mathbf{H}(2a-r_{\alpha\beta}) \right), \end{aligned} \quad (20)$$

where \mathbf{H} is the Heaviside step function and erfc is the complementary error function. Note that the Heaviside term emerges naturally from the inverse Fourier transform and “turns on” the regularization in (9) for overlapping particles (in fact, this is how the regularization was obtained). The “self-term” also emerges naturally from the $r \rightarrow 0$ limit,

$$\langle \psi \rangle_\alpha^s - \psi_0^s(\mathbf{x}_\alpha) = \frac{1}{\epsilon_f} \left(\frac{1 - e^{-4a^2\xi^2}}{8\pi^{3/2}a^2\xi} + \frac{\operatorname{erfc} 2a\xi}{4\pi a} \right) q_\alpha. \quad (21)$$

Note that the point charge result⁵² is recovered by letting $a \rightarrow 0$,

$$\langle \psi \rangle_\alpha^{\operatorname{Re}} - \psi_0^{\operatorname{Re}}(\mathbf{x}_\alpha) = \frac{1}{4\pi\epsilon_f} \sum_\beta q_\beta \frac{\operatorname{erfc} \xi r_{\alpha\beta}}{r_{\alpha\beta}}. \quad (22)$$

The sum of the real space decays exponentially with the distance and can converge rapidly by controlling ξ up to a user-defined cutoff radius, r_c . This truncation leads to an associated truncation error, $\tilde{\delta}_r$, whose bounds can be approximated as⁵³

$$\tilde{\delta}_r \leq C e^{-r_c^2\xi^2}, \quad (23)$$

where C is some constant. The sum of the local interactions on the GPU is performed by assigning one thread per particle and looping through their neighbors. The neighbor list can be handled using a linear complexity linked cell algorithm⁵⁴ which divides the simulation box into cells of size $r_c \sim \xi^{-1}$ and considers interactions only between particles belonging to the same or adjacent cells.⁵⁵

2. Wave-space sum

The wave space contribution to (19) is computed with the spectral Ewald method proposed by Lindbo and Tornberg,⁵² which introduces a parameter η to split the Ewald splitting function, $h(k) = \exp(-k^2/4\xi^2)$, even further,

$$\begin{aligned} \frac{\epsilon_f}{V} \sum_{\mathbf{k} \neq 0} \frac{e^{i\mathbf{k} \cdot \mathbf{x}_\alpha}}{k^2} e^{-k^2/4\xi^2} \sum_\beta q_\beta e^{-i\mathbf{k} \cdot \mathbf{x}_\beta} j_0^2(ka) \\ = \frac{\epsilon_f}{V} \sum_{\mathbf{k} \neq 0} \frac{e^{i\mathbf{k} \cdot \mathbf{x}_\alpha}}{k^2} e^{-(1-\eta)k^2/4\xi^2} j_0^2(ka) \left(\sum_\beta q_\beta e^{-i\mathbf{k} \cdot \mathbf{x}_\beta} e^{-\eta k^2/4\xi^2} \right), \end{aligned} \quad (24)$$

and takes advantage of the fact that the Fourier transform of a Gaussian is a Gaussian, and the shape of this Gaussian is

controlled by η . In particular, for the term in parentheses in (25)

$$\widehat{\mathbf{H}}(\mathbf{k}) \equiv \sum_\beta q_\beta e^{-\eta k^2/8\xi^2} e^{-i\mathbf{k} \cdot \mathbf{x}_\beta}, \quad (25)$$

$$\mathbf{H}(\mathbf{x}) = \left(\frac{2\xi^2}{\pi\eta} \right)^{3/2} \sum_\beta q_\beta e^{-2\xi^2(\mathbf{x}-\mathbf{x}_\beta)^2/\eta},$$

After defining a “scaled” $\widehat{\mathbf{H}}$,

$$\widehat{\widehat{\mathbf{H}}}(\mathbf{k}) \equiv j_0^2(ka) \cdot \frac{e^{-(1-\eta)k^2/4\xi^2}}{k^2} \widehat{\mathbf{H}}(\mathbf{k}), \quad (26)$$

we use Parseval’s formula to compute the rest of the wave-space sum,

$$\begin{aligned} \langle \psi \rangle_\alpha^k - \psi_0^k(\mathbf{x}_\alpha) &= \frac{1}{\epsilon_f V} \sum_{\mathbf{k} \neq 0} \widehat{\widehat{\mathbf{H}}}_\mathbf{k} e^{i\mathbf{k} \cdot \mathbf{x}_\alpha} \\ &= \frac{1}{\epsilon_f} \left(\frac{2\xi^2}{\pi\eta} \right)^{3/2} \int_V d\mathbf{x} \widetilde{\mathbf{H}}(\mathbf{x}) e^{-2\xi^2(\mathbf{x}-\mathbf{x}_\alpha)^2/\eta}, \end{aligned} \quad (27)$$

where $\widetilde{\mathbf{H}}$ is the inverse transform of $\widehat{\widehat{\mathbf{H}}}$.

As in the real space sum (see Sect. III D 1), there is a truncation error for the wave-space sum, $\tilde{\delta}_k$, whose bounds can be approximated as

$$\tilde{\delta}_k \leq C e^{-k_c^2/4\xi^2}, \quad (28)$$

where C is some constant. In our simulations, $k_c \geq |\mathbf{k}|$ corresponds to a real/wave space cubic grid of $N_g = 1 + Lk_c/\pi$ nodes in each dimension with spacing $h \equiv L/N_g$. This regular grid is needed to evaluate fast Fourier transforms (FFTs) and inverse fast Fourier transforms (IFFTs).

As particles’ positions do not tend to perfectly coincide with the points in a regular grid, we need to map the potential and potential gradients from the particle’s positions to nearby points on the grid. This is the role of $\mathbf{H}(\mathbf{x})$, in eq. ??, which uses Gaussians to “spread” or project the particle’s moments on these regular grid points.

The number of grid points over which we extrapolate the information (the potential and its gradients) can be significantly reduced by noticing that $\mathbf{H}(\mathbf{x})$ also decays exponentially. Consequently, we can truncate the spread to a cubic array of the

closest P grid points in each dimension in $O(NP^3)$ calculations, resulting in the truncation error

$$\bar{\delta}_t \leq Ce^{-h^2P^2\xi^2/2\eta}. \quad (29)$$

Similarly, once $\tilde{\mathbf{H}}(\mathbf{x})$ is computed at the grid points via the IFFT of $\hat{\mathbf{H}}(\mathbf{x})$, we interpolate the information from the regular grid points to the particle positions by integrating eq. ?? numerically using the trapezoid rule.⁵⁶ For periodic boundary conditions, the trapezoidal rule quadrature is spectrally accurate⁵² with a quadrature error given by⁵²

$$\bar{\delta}_q \leq Ce^{-\pi^2\eta/2\xi^2h^2}. \quad (30)$$

As FFT and IFFT are accurate up to machine precision,^{56,57} the parameters η and support grid points, P , collectively control the numerical error introduced by the spreading and contracting steps. The natural choice of η ⁵⁸ is obtained by forcing the resulting error from truncating the spreading grid points, $\bar{\delta}_t$, to be equal to the quadrature error, $\bar{\delta}_q$. Thus, we find a simple relation between η and P ,

$$\eta = \frac{h^2\xi^2P}{\pi}. \quad (31)$$

This choice of η ensures that the Gaussian width is wide enough so that the convolution can be easily approximated without incurring unnecessary truncation errors because the Gaussian kernel is not narrow enough. The error for the entire contraction step can be expressed as

$$\bar{\delta}_c \leq Ce^{-\pi P/2}. \quad (32)$$

3. Spectral Ewald implementation

The following algorithm can be used to compute the particle's potential in eq. 19 and potential gradients in each time step. Here, we provide additional details of the GPU implementation of our method (see Supporting Material).

1. Real Space Sum. The sum of the local interactions on the GPU is carried out by assigning one thread per particle and looping through their neighbors. The neighbor's list can be handled using a linear complexity linked cell algorithm which divides the simulation box into cells of size $r_c \sim \xi^{-1}$ and considers interactions only between particles belonging to the same or adjacent cells.⁵⁵

2. Spreading. Divide the simulation box into a Cartesian cubic grid (or over the rectangular domain of the simulation box when the dimensions are unequal) and compute $\mathbf{H}(\mathbf{x})$ using eq. ?? on the grid points. On the GPU, spreading is performed using one block of P^3 threads per particle, with each thread corresponding to one of the P^3 supporting grid points.

3. Fast Fourier Transform FFTs are computed for $\mathbf{H}(\mathbf{x})$ in each Cartesian direction to obtain $\hat{\mathbf{H}}(\mathbf{k})$. Efficient algorithms, such as the NVIDIA cuFFT library,⁵⁹ can perform this operation with $O(N_g^3 \log N_g^3)$ complexity.

4. Scaling. We convert particle moments into potentials in wavespace by scaling $\hat{\mathbf{H}}(\mathbf{k})$ at each of the grid points. Computing $\hat{\mathbf{H}}(\mathbf{k})$ requires $O(N_g^3)$ operation and a single execution thread is assigned to each point in the grid.

5. Inverse Fast Fourier Transform. As with the FFT step, we compute $\tilde{\mathbf{H}}(\mathbf{x})$ on the grid points. This step requires $O(N_g^3 \log N_g^3)$ operations.

6. Contraction. We interpolate $\tilde{\mathbf{H}}(\mathbf{x})$ from the equally spaced grid points to the particles' positions using Gaussians to arrive to ??, evaluated numerically using quadrature *via* the trapezoidal rule. Finally, we add the contributions to the potential and its gradients from the real and imaginary parts.

IV. POLARIZABLE COLLOIDS IN AN EXTERNAL ELECTRIC FIELD

In this section, we demonstrate our immersed boundary method on four test problems of static configurations of polarizable colloids where exact solutions are known.

A. Single sphere in an electric field

A single ideally polarizable spherical particle of radius a_b in a uniform electric field \mathbf{E}_0 acquires a dipole moment

$$\hat{\mathbf{S}} = 4\pi a_b^3 \epsilon_f \mathbf{E}_0, \quad (33)$$

In figure 1, we compare the dipole moment \mathbf{S} computed from (15) using our immersed boundary method on an icosphere of N constituent beads to the exact $\hat{\mathbf{S}}$. The relative error, $\bar{\delta} = \|\mathbf{S} - \hat{\mathbf{S}}\| / \|\hat{\mathbf{S}}\|$, decays slowly as $\bar{\delta} \sim N^{-1/2}$, but an error of about $\approx 5\%$ is obtained for $N \approx 1000$. One contributing factor to this error is the fact that, because tessellating beads have finite radii a , the total radius of the icosphere is larger than the radius of the particle sphere a_b on which the bead centers lie. We define an effective radius a_{eff} of the icosphere based on the calculated induced dipole, $\mathbf{S} = 4\pi a_{\text{eff}}^3 \epsilon_f \mathbf{E}_0$, which depends on N . Figure 1(c) shows the relative difference between a_{eff} and a_b for icospheres of different N . This difference is largest for small N , where the tessellating bead radii are comparable to the particle radius, and $a_{\text{eff}} \rightarrow a_b$ as the number of constituent beads increases and their radii decrease. Note that because a_{eff} is always larger than a_b , the icosphere dipole \mathbf{S} has a larger magnitude than $\|\hat{\mathbf{S}}\|$. We prevent the errors from this single body calculation from propagating through subsequent calculations involving multiple particles by using a_{eff} as the particle radius rather than a_b .

B. Pair of spheres in an electric field

The dipoles of a pair of ideally polarizable spherical particles with radius a_b in an external field \mathbf{E}_0 (fig 2a) can be expressed as a power series in inverse distance^{60,61}

$$\hat{\mathbf{S}} = 4\pi a_b \epsilon_f \sum_{p=0}^{\infty} \left(\frac{a_b}{r}\right)^p (A_p \mathbf{I} + B_p \hat{\mathbf{r}}\hat{\mathbf{r}}) \cdot \mathbf{E}_0, \quad (34)$$

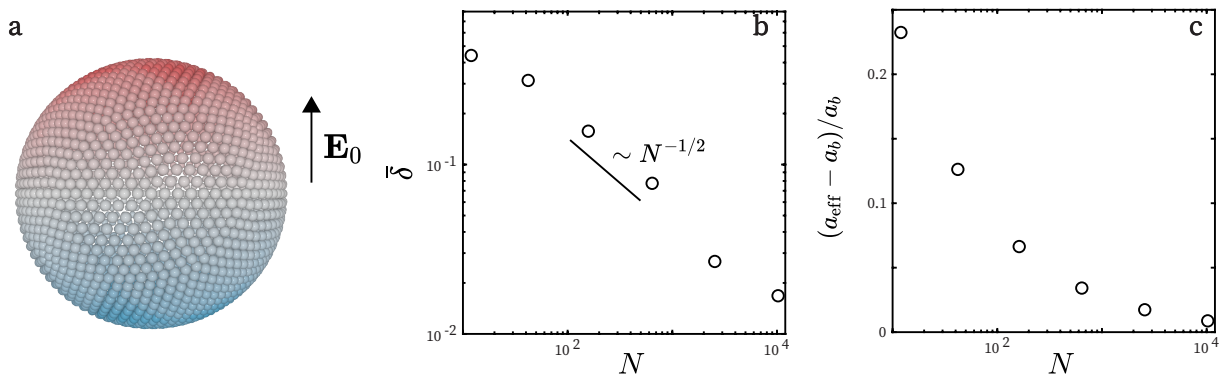


Figure 1. (a) Snapshot of an ideally polarizable sphere comprised of $N = 2562$ beads in an electric field \mathbf{E}_0 . The induced charge distribution obtained from our immersed boundary method is indicated by the color intensity, with red and blue indicating positive and negative charges, respectively. (b) Relative error $\delta = \|\mathbf{S} - \hat{\mathbf{S}}\|/\|\hat{\mathbf{S}}\|$ between the particle dipole \mathbf{S} obtained from our immersed boundary method and the exact dipole $\hat{\mathbf{S}}$ in (33) as a function of the number of constituent beads N . (c) Relative difference between the effective radius a_{eff} and the true particle radius as a function of N .

where \mathbf{r} is the center-to-center vector, $r = \|\mathbf{r}\|$, $\hat{\mathbf{r}} = \mathbf{r}/r$, \mathbf{I} is the identity tensor, and A_p and B_p are coefficients found in eqs. 5.6 through 5.8 in ref.⁶¹. The force on each particle is related to the gradient of the dipole strength,

$$\hat{\mathbf{F}} = -\nabla \hat{\mathbf{S}} \cdot \mathbf{E}_0. \quad (35)$$

Figure 2 shows the dipole and force on the pair of spheres computed using our immersed boundary method as a function of the distance r and the number of tesselling beads N . The solid lines represent the analytical values computed by using eqs. 34 and 35. Each distance point represents the average value of ten independent angular configurations for the spheres to avoid any bias introduced by the alignment of beads belonging to different bodies. However, the spread of the values at each point is small enough such that they would fall inside the markers and, therefore, is not depicted. When scaled on the effective radius, the dipole and force are in good agreement with the exact solution for a pair of spheres.

Unlike the single-sphere case described in section IV A, the charge distribution for each of the composite spheres is not symmetric about the equator. Instead, the induced charge distribution is mostly localized in the region close to the other sphere. Moreover, as the distance between surface over which the charge is distributed the dipole dramatically increases, indicating the preferred conduction path.²⁹ Both of these important features are shown when using the immersed boundary method with expected small deviations present for $N = 42$ and only when the surface-to-surface distance is smaller than the radius of the composing bead, a . In the absence of hard steric repulsions, the regularization for ψ_α in eq. 7 facilitates the computation of numerically finite charge distributions of overlapping polarizable bodies. This is the case for the computed dipoles in fig. 2 b for values of $r < 2a_b$. In contrast, finite element-type methods are ill-equipped to estimate the induced charge of overlapping polarizable shells resulting in unphysical charge distributions. In dynamic simulations, where hard repulsions cannot be represented exactly, small overlaps are common, which makes it difficult to use finite element meth-

ods directly on configurations obtained from simulation.

C. Cubic array of spheres in an electric field

To this point, we have only considered systems with a finite number of spheres. However, our goal is to take advantage of the computational method to simulate suspensions with an infinite number of particles. The simplest case is given by a periodic array of bodies. This type of two-phase media is prevalent in composite materials, and a well-studied quantity is the effective conductivity of media.^{28,46,61} For suspensions of ideally polarizable bodies, this conductivity is the effective permittivity of the suspension, ϵ_{eff} .²⁹

We compute the effective permittivity from the elements of the grand capacitance tensor in eq. 15 as proposed by Bonnetaze and Brady.⁴⁶ That is

$$\epsilon_{\text{eff}} = \epsilon_f - n \langle \mathbf{C}_{S\Psi} \cdot \mathbf{C}_{q\Psi}^{-1} \cdot \mathbf{C}_{qE} - \mathbf{C}_{SE} \rangle, \quad (36)$$

where ϵ_f is the conductivity of the particle surroundings, and $\langle \dots \rangle$ is an average over all the bodies. The permittivity is commonly present in the tensorial form, but for an isotropic configuration, it is just a scalar value, $\epsilon_{\text{eff}} \mathbf{I}$. Each of the terms inside the angle brackets are the couplings between the moments of the particles and the potential and its gradients, and form the matrix

$$\mathbf{C} = \begin{bmatrix} \mathbf{C}_{q\Psi} & \mathbf{C}_{qE} \\ \mathbf{C}_{S\Psi} & \mathbf{C}_{SE} \end{bmatrix}. \quad (37)$$

In a periodic cubic array, the couplings \mathbf{C}_{qE} and $\mathbf{C}_{S\Psi}$ are zero.⁴⁶ Thus, the average dipole of the cubic array is the same as the dipole of a single sphere in a periodic cell, that is, $\epsilon_{\text{eff}} = \epsilon_f + n \langle \mathbf{C}_{SE} \rangle$.

To assess the validity of the computed permittivities, we use Sangani and Acrivos results²⁸ for the effective conductivity for cubic arrays of spheres as a function of the volume fraction.

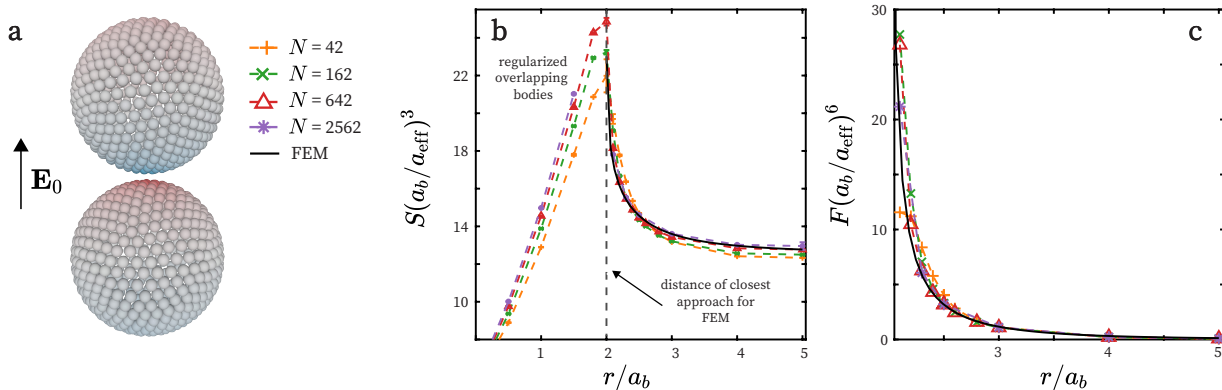


Figure 2. (a) Pair of ideally polarizable spheres in the presence of an external field \mathbf{E}_0 . The charge distribution is qualitatively shown by color: positive and negative charges are depicted in red and blue, respectively. The saturation of the color is proportional to the absolute value of the bead’s charge. (b) Computed dipole moment scaled in the effective radius of the body as a function of the center-to-center distance in units of the radius of the bodies, a_b . Results are shown for different levels of refinement ($N = [42, 162, 642, 2562]$). Values obtained by the expansion in Eq. 34 and recursions for the weighting coefficients in ref.⁶¹ are shown as a solid black line and are equivalent to the Finite Element Method. Notice how the regularization of the charge over the surface of the rigid bodies allows for particles to overlap, that is, $r < 2a_b$, without diverging. (c) Evolution of the attractive force, scaled on a_{eff} , on the spheres as the distance between them increases. The solid black line is the force obtained using eqs. 34 and 35.

Figure 3 (a) shows the effective permittivity in units of the fluid permittivity as a function of the volume fraction for a simple cubic array. At low concentrations, $\phi \leq 0.15$, good accuracy is obtained even for the bodies comprising a few beads. As the concentration of the bodies increases, the interparticle distance decreases and the interactions between the image bodies in the simulation cell become important. Nonetheless, good accuracy is obtained for bodies comprising $O(100)$ or more. At significantly high concentrations $\phi \geq 0.40$, only bodies comprising $O(1000)$ are in close agreement with the behavior predicted by Sangani and Acrivos. Near the simple cubic maximum packing limit (vertical gray dotted line in fig. 3 (a)) it is expected that the dipole, and consequently the effective permittivity, will diverge. Although all the composite spheres show a significant increase in the effective conductivity as we approach the packing limit, a completely accurate result would require an infinite number of moments in equation 8 which would noticeably decrease the efficiency of the method.

Furthermore, we computed the effective permittivity for a face-centered cubic (FCC) array from dilute to closest packing. A snapshot of one cell in the lattice is seen in figure 3 (b). The results show a similar trend to the simple cubic array, the main difference being that the closest packing for SC (indicated by the vertical dotted gray line in figs 3 (a) and (c)) is significantly lower than for FCC.

The GPU time complexity of our method is obtained by tracking the time required to compute the induced charge distribution for a series of FCC array configurations in an electric field using GeForce GTX 1080 graphics card by Nvidia. The level of refinement and the total number of simulated bodies varied from $N_b = 8$ (two bodies in each dimension) to $N_b = 512$ (eight bodies in each dimension). The Ewald splitting parameter was set to $\xi = 0.5$ and Spectral Ewald parameter, η chosen to commit to an error tolerance of 10^{-3} by re-

lating it to the Fourier transform number of grid nodes, P , and spacing, h , via $\eta = P(h\xi)^2/\pi$.⁴⁷ The obtained computational times are depicted in fig. 3 (d) as a function of the total number of beads in the simulation box $N_T = N \times N_b$. The distribution of elapsed times shows a time complexity $O(\sqrt{N_T} \log N_T)$ for simulations containing up to $O(10^5)$ beads. Although log linearity is reached for larger systems, the time required to obtain the charge distribution of simulations containing up to $O(10^6)$ beads remains within one second.

D. Rigid rod in an electric field

Colloidal particles are present in a variety of topologies. Our immersed boundary method is not only applicable to spherical bodies, but can include other geometries as well. Consider, for example, a long but slender ideally polarizable body, hereafter simply a “fiber”, immersed in an external electric field.

The fiber’s geometry can be approximated by a variety of structures. For the purpose of this discussion, we approximate the body by four parallel lines of particles composing a single fiber. The anisotropy of the fiber is controlled by the ratio of the longest to the shortest axis, χ . Figure 4 (c) shows this structure in the presence of an external field.

While we are not aware of the existence of an exact solution for this particular geometry, we expect the dipole moment and torque on the fiber to converge to that of a prolate spheroid for large values of χ . The dipole moment of an ideally polarizable body can be found via the relation⁶²

$$\mathbf{S} = [\mathbf{I} - \mathbf{A}^*]^{-1} \cdot \mathbf{E}_0; \quad \mathbf{A}^* = \begin{bmatrix} Q & 0 & 0 \\ 0 & Q & 0 \\ 0 & 0 & 1 - 2Q \end{bmatrix}. \quad (38)$$

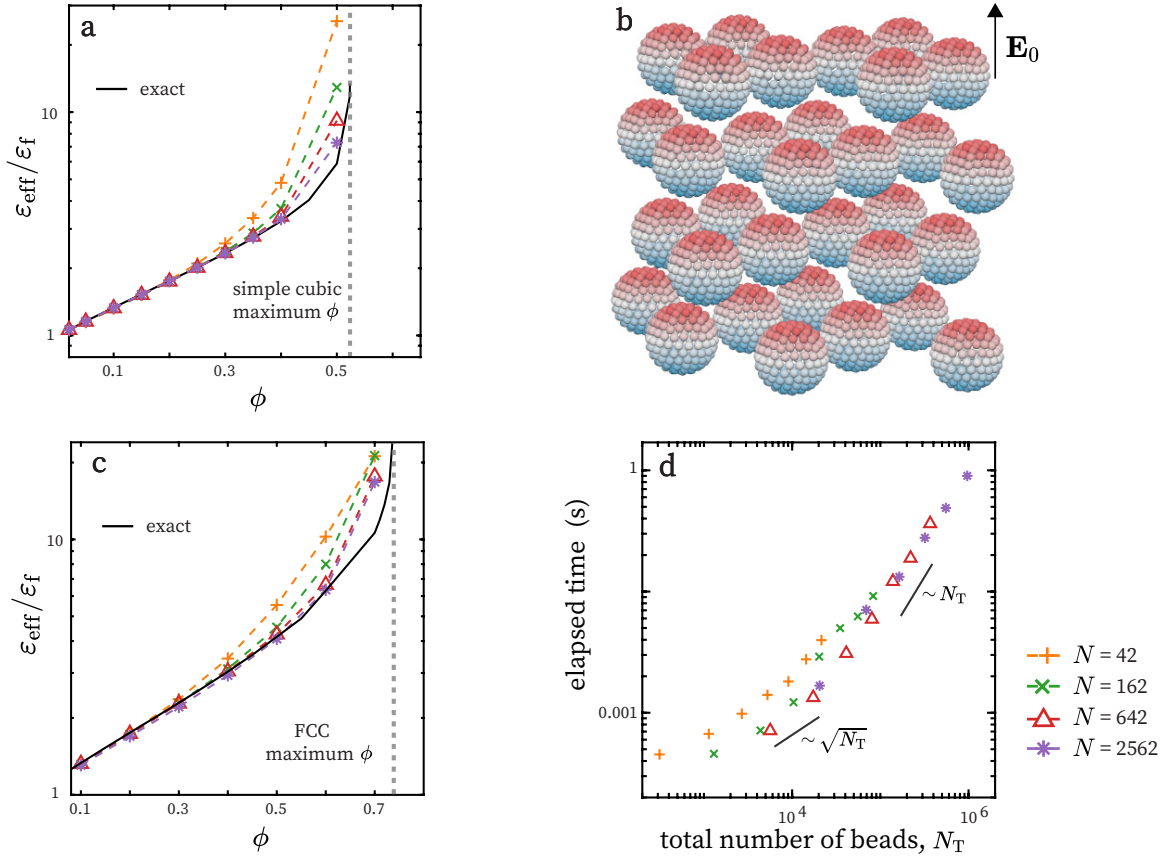


Figure 3. (a) Effective permittivity for a periodic simple cubic array of ideally polarizable bodies as a function of the volume fraction of the bodies. The number of beads, N , decreases in the downward direction ($N = [42, 162, 642, 2562]$). The solid black line represents the results obtained by Sangani and Acrivos²⁸ for a simple cubic lattice. (b) FCC lattice of ideally polarizable spheres in the presence of an electric field \mathbf{E}_0 . The positive and negative induced charges are shown in red and blue, respectively. The saturation of the color is proportional to the magnitude of the bead charge. (c) Effective permittivity for an FCC configuration of ideally polarizable bodies in the presence of an external field. The number of beads composing the bodies increases in the downward direction ($N = [42, 162, 642, 2562]$). The black solid line shows the results obtained by Sangani and Acrivos for an FCC configuration of inclusions.²⁸ The dashed vertical lines in (a) and (c) correspond to the simple cubic lattice packing limit, $\phi \approx 0.52$, and FCC lattice packing limit, $\phi \approx 0.74$, respectively. (d) Elapsed time per time step as a function of the total number of beads, $N_T = N_b \times N$ for FCC lattice configuration. The number of bodies in the simulation box increases to the right, $N_b = [8, 27, 64, 125, 216, 343, 512]$

Where \mathbf{A}^* is known as the depolarization tensor,⁴⁴ and Q for a prolate spheroid is given by

$$Q = \frac{1}{2} \left\{ 1 + \frac{1}{(b/a)^2 - 1} \left[1 - \frac{1}{2\chi} \log \left(\frac{1+\chi}{1-\chi} \right) \right] \right\}. \quad (39)$$

Figure 4 (a) and (b) show the induced dipole moment on the fiber, S , and the resulting torque, $\Gamma = \mathbf{S} \times \mathbf{E}_0$ as a function of the angle between the applied field and the longest axis of the fiber. The ratio of the longest to the smallest axis, χ , ranges from $\chi = 5$ to $\chi = 40$. Solid lines represent the computed dipole moments and torques using eq. 38. Notice that the induced dipole moment in the direction of the field is at its maximum when the field and the longest axis are parallel to each other ($\theta = 0$) and decreases to zero when they are orthogonal to each other ($\theta = \pi/2 = 90^\circ$). Furthermore, the maximum of the torque, fig. 4 (b) is found at values of $\theta = \pi/4 = 45^\circ$ as expected for this geometry. At low values of χ , significant differences are obtained between the dipole

moment computed by the simulations and the dipole moment obtained by the polarization tensor. This is a result of the geometrical dissimilarities between our approximated fiber and the prolate spheroid. Nonetheless, as the ratio, χ , increases in value, the far-field of both structures tends to the same dipole and torque, which corresponds to the limit where these dissimilarities are small.

V. BROWNIAN DYNAMICS SIMULATIONS OF CHARGED AND POLARIZABLE COLLOIDS IN EXPLICIT ELECTROLYTES

The numerical computations presented in IV provide information on the numerical accuracy of our immersed boundary method when computing single- and multibody properties of equally sized bodies. However, the primary goal of our simulation method is to accurately and efficiently simulate electro-

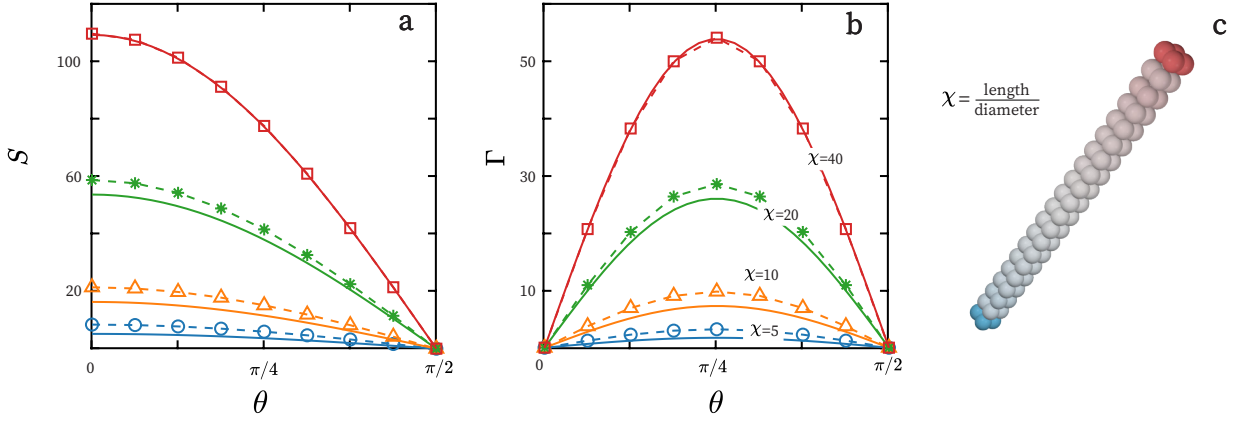


Figure 4. Evolution of the (a) induced dipole moment in the direction of the external electric field and (b) resulting torque as a function of the angle between the applied field and the longest axis of the fiber at different values of aspect ratio, χ . The aspect ratio increases in the upwards direction. Values corresponding to $\chi = 5$, $\chi = 10$, $\chi = 20$ and $\chi = 40$ are represented by circled (in blue), triangled (in orange), starred (in green), and squared (in red) markers, respectively. The solid lines in panel (a) and (b) are computed using the depolarization tensor, as in eq. 38, for a prolate spheroid.⁶²

statically stabilized colloidal suspensions. In this section, we will study the method in the context of Brownian Dynamics simulations of colloidal particles in the presence of an explicit electrolyte. First, we show the equilibrium structural properties of the electric double layer for a negatively charged colloidal particle in an explicit electrolyte. Then we demonstrate the applicability of the method to obtain transport properties of colloidal suspensions by computing the electrophoretic velocity of charged colloids and studying the electrokinetic phenomenon known as “induced-charge electroosmosis”.⁶

A. Brownian dynamics

We model the ions and counterions in the electrolyte as a suspension of charged, hard, spherical particles. We will interchangeably refer to them as “beads.” Colloidal particles are constructed as explained in Section III and we will commonly call them “bodies.” The solvent is treated implicitly and is assumed to be Newtonian, so that it interacts with the ions through hydrodynamic forces from flows in the medium and stochastic Brownian forces due to momentum relaxation of the solvent molecules.⁶³ On the colloidal scale, inertial relaxation occurs on time scales orders of magnitude smaller than those on which the ions move. In this regime, any perturbation to ion momentum is felt almost instantaneously, which causes the ions to move at its terminal velocity. Under these assumptions, inertial effects can be ignored and the overdamped Langevin equation governs the dynamics of the ions:⁶³

$$0 = \mathbf{F}_\alpha^H + \mathbf{F}_\alpha^I + \mathbf{F}_\alpha^E + \mathbf{F}_\alpha^B, \quad (40)$$

where \mathbf{F}_α^H is the hydrodynamic force acting on the α^{th} ion, \mathbf{F}_α^I accounts for forces arising from a generic conservative potential, \mathbf{F}_α^E is the external force exerted by a global electric field⁴⁷ and \mathbf{F}_α^B is the stochastic Brownian force. The last force satisfies the fluctuation-dissipation theorem³ with ensemble aver-

age:

$$\begin{aligned} \langle \mathbf{F}^B(t) \rangle &= 0; \\ \langle \mathbf{F}^B(t) \mathbf{F}^B(t + \tau) \rangle &= 2k_B T (\mathbf{M}^H)^{-1} \delta(\tau), \end{aligned} \quad (41)$$

where $\mathbf{F}^B(t) = [\mathbf{F}_1^B(t), \mathbf{F}_2^B(t), \dots]$, $\langle \cdot \rangle$ indicates the expectation value, δ is the Dirac delta function, and \mathbf{M}^H is the hydrodynamic mobility tensor. This formulation ensures that any energy an ion gains from a thermal fluctuation is dissipated as drag to the solvent.

The hydrodynamic mobility tensor couples the non-hydrodynamic force, $\mathbf{F}_\beta = \mathbf{F}_\beta^I + \mathbf{F}_\beta^E + \mathbf{F}_\beta^B$, to the velocity of the α^{th} ion:

$$\mathbf{u}_\alpha(t) = \sum_{\beta=1}^N \mathbf{M}_{\alpha\beta}^H \cdot \mathbf{F}_\beta(t). \quad (42)$$

For simplicity, we will neglect interparticle hydrodynamic interactions, but these can be included using the Rotne-Prager-Yamakawa mobility tensor.²² Thus, the drag on each ion is decoupled from all the others and is equal to the Stokes drag,

$$\mathbf{M}_{\alpha\beta}^H = 0, \alpha \neq \beta; \quad \mathbf{M}_{\alpha\alpha}^H = \mathbf{I}/\gamma, \quad (43)$$

where all ions are assigned the same drag coefficient, γ . Equation 40 can be solved numerically via a Euler-Maruyama integration scheme:

$$\mathbf{x}_\alpha(t + \Delta t) = \mathbf{x}_\alpha(t) + \mathbf{u}_\alpha(t) \Delta t, \quad (44)$$

where Δt is the time step over which the ion trajectories advance.

Forces arising from conservative interactions among ions are represented as the gradient of a potential energy $U(\mathcal{X})$, which is a function of the coordinates of all ions $\mathcal{X} \equiv [\mathbf{x}_1, \mathbf{x}_2, \dots, \mathbf{x}_N]^T$,

$$\mathbf{F}_\alpha^{I/E}(\mathcal{X}) \equiv -\nabla_{\mathbf{x}_\alpha} U^{I/E}(\mathcal{X}), \quad (45)$$

where the gradient is taken with respect to the position of the α^{th} particle.

In our analysis, we are concerned with finite sized ions, which cannot overlap. The hard-sphere force computed by the derivative of the well-known step-like potential is discontinuous; it is zero everywhere except for a δ -function of infinite magnitude at contact. This type of potential cannot be implemented directly in simulations. Typically, the hard potential is approximated with a soft potential of the form r^{-n} , where n is a large power. The larger n is, the more accurately the soft potential approximates the hard potential, but the resulting force becomes larger as the potential diverges increasingly rapidly.⁶⁴ Smaller time steps must therefore be taken as n increases to prevent unphysically large steric forces, rendering this method computationally inefficient. Heyes and Melrose implemented a "potential-free" hard sphere algorithm by allowing particles to overlap over the course of a time step because of other forces and then separating them to contact at the end of the time step.⁶⁵ Because equations (42) and (44) give a relation between particle displacements and forces, we can compute the effective force required to move two overlapping ions back into contact after one time step. Thus, the potential-free algorithm can be equivalently written in terms of a hard sphere pair potential.⁶⁶

$$U_{\alpha\beta}^{\text{hs}}(r) = \begin{cases} \frac{\gamma}{4\Delta r}(r-2a)^2 & \text{if } r < 2a \\ 0 & \text{if } r \geq 2a \end{cases}, \quad (46)$$

where a is the hard-sphere radius of an ion. In the form of the potential used here, γ and a are the same for all particles.

All simulations are of colloids immersed in the binary and symmetric electrolyte; that is, ions of different species have the same charge in magnitude but opposite in sign. Distance and time are made dimensionless by measuring distances relative to the radius of the ion, a , and time relative to the diffusion time of the ion, $\tau_D = k_B T / \gamma a^2$. The charge scale is set by $\sqrt{\epsilon_f a k_B T}$. The volume fraction of the colloids, ϕ_b , and the length of the simulation box are the same in all simulations and given by $\phi_b = 0.01$ and $L = 108a$, respectively. The charge of the ions, q_i , is prescribed by the dimensionless parameter ϵ (different from the permittivity of the solvent, ϵ_f). We define this quantity as the electric potential between two charges at contact with respect to the thermal energy,

$$\epsilon = \frac{q_i^2}{8\pi\epsilon_f a k_B T}. \quad (47)$$

The presented values of the electrostatic interactions relative to $k_B T$ are chosen to be within the range of values commonly found in common electrolytes: $\epsilon = [0.5, 2.0]$. For example, for a solution of NaCl in water at room temperature, $\epsilon \approx 1.1$ (assuming relative permittivity of 80). The ratio of the charge in the colloid with respect to the ions is given by $\sigma = Q/(Nq_i)$, where Q is the total charge in the colloid and N the number of beads that compose the body. The charge in the colloid needs to be balanced by σN counter-ions to ensure electroneutrality. Simulations were at least $200\tau_D$ long and the first $100\tau_D$ are discarded to ensure equilibrium. The integration time-step was $10^{-3}\tau_D$ and of equal value in all simulations.

B. Electric double layer around a charged colloid

Our immersed boundary method can be used to identify important features of electrostatically stabilized colloidal suspensions. We illustrate some of our method's capabilities by studying the structure of the electric double layer present on the colloid-solvent interface. Figure 5 (a) shows a snapshot of a negatively charged colloidal particle in an explicit electrolyte, where some of the ions are not shown, allowing qualitative details of the counterion cloud to be easily observed. The counterions generally try to balance the charged colloid and acquire electroneutrality. Using the positions of the ions, we can gain some insight into the charge density distribution, $\rho(\mathbf{r})$, and consequently verify the electroneutrality of the simulation box. Figure 5 (b) shows the cumulative charge density,

$$Q'(r) = Q + \int_{a_b}^r \langle \rho(r') \rangle dr', \quad (48)$$

at different ion volume fractions, $\phi_\infty = [0.05, 0.25]$. The strength of the ion-ion interactions at contact for the simulations shown was set to $\epsilon = 0.5$ in units of the thermal energy, $k_B T$. The colloid is made up of 642 beads, has a radius of $a_b \approx 14.5a$ and $\sigma = 1.0$. Solid lines show the expected behavior of the Debye-Huckel-Stern theory,³ where the Stern layer thickness was left as a fitting parameter.

The local charge densities required to compute $Q'(r)$ are found by discretizing the space surrounding the colloid into consecutive shells. The average local charge at each of the discretization points, $\langle \rho(r) \rangle$, was found using a sliding window algorithm.⁶⁷ We chose the window to be twice the radius of the ion and the discretization steps equal to $0.1a$.

Consistent with the screening of electrostatic interactions, the decay of the cumulative charge is proportional to the volume fraction of the ions ($\phi_\infty = [0.05, 0.25]$). Notice significant differences between the computed cumulative charge using Debye-Huckel-Stern theory, and that computed from the simulations, particularly at high concentrations where screening effects give rise to long-range charge density oscillations⁶⁸.

While the cumulative charge and other integrated quantities (such as capacitance) can be well estimated using local density approximations to obtain the charge density distribution of the ionic species near charged surfaces,^{69,70} to our knowledge, these cannot correctly represent structural features on the order of the ion diameter of the double layer structure. The local microscopic density or structure of a liquid (and other states of matter in other contexts) is better characterized by the partial pair correlation function, which for species ν and μ is defined as:⁷¹

$$g_{ij}(\mathbf{r}) = \frac{1}{V n_i n_j} \left\langle \sum_{\alpha=1}^{N_i} \sum_{\beta \neq \alpha}^{N_j} \delta(\mathbf{r} + \mathbf{r}_\alpha - \mathbf{r}_\beta) \right\rangle, \quad (49)$$

where $\mathbf{r}_{\alpha/\beta}$ is the position of particle α of species i or of particle β of species j . In single-component systems, particles α and β belong by definition to the same species. For multicomponent systems, the species i and j can represent the same or different species.

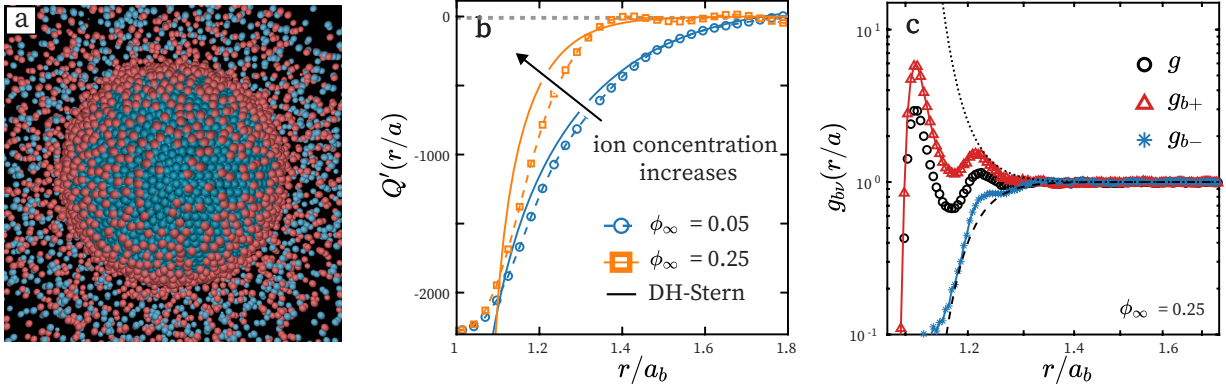


Figure 5. (a) Snapshot of charged colloid in an electrolyte depicting counterions being attracted to the surface of the colloidal particle (some ions were removed for clarity). Positively charged and negatively charged species are shown in red and blue. (b) Cumulative charge density, as present in eq. 48, from dynamic simulations of negatively charged colloid in an explicit electrolyte at different ion volume fractions. Circles in blue and squares in yellow represent concentrations of $\phi = 0.05$ and $\phi = 0.25$, respectively. Solid lines represent the expected cumulative charge distributions computed using Debye-Huckel theory and considering the Stern layer; the Stern layer thickness was left as a fitting parameter. (c) Colloid-ion correlation functions (black markers), colloid-counterion (solid red line with triangular markers), and colloid-co-ion pair correlation functions at different ion volume fractions showing the microstructure of the double layer at $\phi = 0.25$. Dotted and dashed lines show the expected colloid-counterion and colloid-co-ion pair correlation functions, respectively. The distributions are computed by assuming that the pair correlation function can be approximated by $g_{ij} \sim \exp(-U_{ij}(r))$.

Figure 5 (c) presents an example of the pair correlation functions between 1) the colloid and all ionic species, $g(r)$, 2) colloid and counterions, $g_{b+}(r)$, and 3) colloid and coions, $g_{b-}(r)$ for volume fractions of $\phi_{\infty} = 0.25$. The pair correlation function is obtained using the standard “shell summation” method⁵ averaged over 50 uncorrelated configurations over time. The simulation’s results are compared against the values obtained by approximating the pair distribution function to be $g_{ij} \sim \exp(-U_{ij}(r))$.⁷² The interparticle potential, U_{ij} , is a screened Coulomb potential between two small charged molecules.² This approximation for the partial pair correlation function is only valid in the low concentration regime and in the limit of $r \gg a_b$, so deviations near the surface of the colloidal particle are expected. The first peaks of g and $g_{b,+}$ (shown in red and black markers), are approximately located at the distance of closest approach between the ions and the colloidal particle ($r \approx 16.5a$ or $r \approx 1.1a_b$). A second shell of counterions (located at $r \approx 18.5a$ or $r \approx 1.2a_b$) surrounding the colloid is also present. The colloid-co-ion pair correlation function shows a depletion of like-charged ions near the surface of the colloid. Note that g_{b-} is nonzero for values of $r \approx 1.15a_b$; as screening effects and excluded volume interactions become important, the repulsive force between the colloid and the like charged ion is opposed by additional osmotic forces from the surrounding ions, likely giving rise to this nonzero value of g_{b-} .

C. Induced-charged electrophoresis

When the colloidal particle has a non-zero net surface charge, the presence of an external electric field will cause the

colloidal particle to translate in the electrolyte with a velocity,

$$\mathbf{U} = \frac{\epsilon_f \zeta_0}{\mu} \mathbf{E}_0, \quad (50)$$

where ζ_0 is the net zeta potential and μ is the solvent viscosity. Eq. 50 holds if the electric double layer thickness is significantly smaller than the sphere radius; that is, the thin double layer limit. Figure 6 (a) shows the electrophoretic velocity for a colloidal particle in an electrolyte for different charge densities. The filling fraction of the electrolyte is $\phi_{\infty} = 0.10$ and the radius of the rigid body, a_b , is approximately $29a$ (or $N = 642$ composing beads). As expected, the velocity obtained in the simulations increases with the applied electric field and the charge density. Importantly, the predicted electrophoretic velocity from eq. 50, depicted by the solid lines, is in close agreement with the simulations for the lowest charge densities (starred and squared markers), which is the limit where this equation is valid. The highest charge density values (triangled and circled markers) show greater deviations from the ideal solution velocity, likely due to particle and double layer convection. In the presence of an applied electric field, polarizable colloidal particles acquire a non-uniform surface charge distribution in addition to its fixed charge. When surrounded by ions in solution, positive ions are drawn toward the particle’s negative induced charges, while negative ions are drawn toward the positive induced charges on the surface of the colloid. That is, the ion cloud of the colloid also polarizes, as seen qualitatively in the ion cloud distribution in Fig. 6 (b). The overabundance of ionic species near the surface of the colloid creates an *additional* potential gradient. This ion-dense fluid contributes further to the polarization of the colloid. During this process, the colloidal particles and the double layer region “charge up” over time. The charge distribution emanates a

quadrupolar flow field in the surrounding fluid. The charging dynamics can be explained using Squire and Bazant’s electrokinetic theory of “induced-charge electroosmosis” (ICEO) phenomenon.^{6,43} Assuming ideal solution behavior, the charging time and dipole moment are found to be

$$\tau_c = \frac{\epsilon_f \kappa_D a_b}{2\sigma_i(1 + \kappa_D a)}; \quad \frac{S}{S_0} = 1 + \frac{\kappa_D a_b}{2(1 + \kappa_D a)}; \quad (51)$$

where σ_i is the ionic conductivity, different from the ratio of the colloid bead charge to the ion charge, σ .

This electrokinetic phenomenon behaves differently from classical electrophoresis due to the presence of the polarized double layer, which negatively aligns with the external field. In fact, this polarizable double layer becomes unstable above a certain critical electric field. Small thermal fluctuations can break the symmetry of the polarized ion cloud and result in a spontaneous rotation of colloidal particles in the orthogonal direction of the applied field.^{73,74} This spontaneous rotation is known as the Quincke rotation⁷⁵. When coupled with the motion of induced charge electrophoresis, this phenomenon is analogous to the “Magnus effect” at larger Reynolds numbers. Here, we limit our analysis to applied electric fields below the instability threshold, but the Immersed Boundary Method described in this document has previously been used to study the “electrokinetic magnitude effect”.⁷⁴

We performed simulations at various discretization levels and followed the dependence of the dipole moment of the particle as a function of the magnitude of the applied field. Figures 6 (c) and 6 (d) show the final dipole strength and charging time, τ_c , in units of τ_D as a function of the applied field scaled on the electric field scale set by ϵ_f , $\sqrt{k_B T/a^3 \epsilon_f}$. The blue circled, yellow starred and green squared markers represent the values obtained from colloidal particles of radius $a_b \approx 14.5a$ (composed of $N = 642$ beads), $a_b \approx 29a$ (composed of $N = 2562$ beads) and $a_b \approx 57.8a$ (composed of $N = 10,242$ beads), respectively. Solid lines correspond to the dipole moment and charging time computed using eq. 51 and Debye-Huckel-Onsager relation for the ionic conductivity conductivity.⁷⁶ It can be seen in the plots that the simulations and the ICEO model agree qualitatively. Figure 6 shows the particle dipole and the charging time for particles with various net charges from simulation and Carnahan-Starling theory. As the differential capacitance decreases with ζ and q grows slowly,⁴⁷ particles with a net charge begin with a lower capacitance than a charge-free particle and charge less strongly. Both the dipole strength and the charging time decrease with σ at small $\tilde{E}_0 = E_0/\sqrt{k_B T/a^3 \epsilon_f}$. In fact, charging is nearly completely suppressed for the largest σ tested. The net charge is important when its associated zeta potential is comparable to or greater in value than the induced zeta potential, $\zeta_0 \gtrsim aE_0$. As E_0 increases, the induced ζ dominates the net ζ_0 and all the net charged particles behave the same.

VI. CONCLUSION

We have presented an immersed boundary method for simulating equilibrium and dynamic properties of charged and/or

polarizable colloidal dispersions. Our method utilizes a Spectral Ewald summation and is parallelized for computation on GPUs, allowing for robust error control while efficiently scaling to $O(10^6)$ beads. We have shown that our method is a useful tool for modeling a variety of soft electrokinetic materials, including collections of polarizable colloidal particles (Sec. IV A -IV C) and anisotropic (Sec. IV D) colloidal particles in electric fields, ionic double layers around charged colloids in electrolytes (Sec. V B), and ion and colloid dynamics of electrolytic dispersions under an applied voltage (Sec. V C).

We have computed the pair correlation functions and charge density distribution of the electric double layer in which our simulations show similar behavior to mean-field treatments of the electrolyte in the region where ideality assumptions are valid (low concentration, weak electrostatic interactions). Importantly, we find qualitative and quantitative improvements over those obtained from mean-field simulations for concentrated and highly correlated systems where long-range ordering of the charge density distribution arises. The method is able to accurately estimate transport properties of electrostatically stabilized colloidal dispersions and accurately represent nonlinear electrokinetic phenomena. To the best of our knowledge, existing particle-based methods look only at the equilibrium fluctuations via Green-Kubo relations to obtain transport properties of the charged species.^{77,78} Nonetheless, the transport coefficients obtained from simulations near equilibrium cannot be used to predict the response to alternating electric fields, nor do they consider any induced-charge polarization effects (such as induced charge electrophoresis).⁶ Finally, an existing GPU-capable molecular dynamics package, HOOMD,⁷⁹ was leveraged for thermodynamic modeling of rigid assemblies and data handling. A plug-in for HOOMD can be found in the supporting material distributed under the GPL license, which can be used to validate all of the shown results. Moreover, the plug-in can be used to provide a reliable picture of structural and transport properties of particles of arbitrary shape, such as rigid rods and rings. Overall, our spectrally accurate GPU-driven immersed boundary method for simulations of ideally polarizable bodies is optimal for particle-based simulations of charged soft matter system with simulation boxes comprising anywhere from a few thousand to low millions beads.

SUPPORTING MATERIAL

The data that support the findings of this study are available from the corresponding author upon reasonable request. The plug-in can be downloaded in <https://github.com/Swan-Group-Code/ConductorRigid> by accessing the following URL: <https://github.com/Swan-Group-Code/ConductorRigid>

ACKNOWLEDGMENTS

We wish to thank Alfredo Alexander-Katz, Madhu Majji, and Martin Z. Bazant for their helpful discussions. We

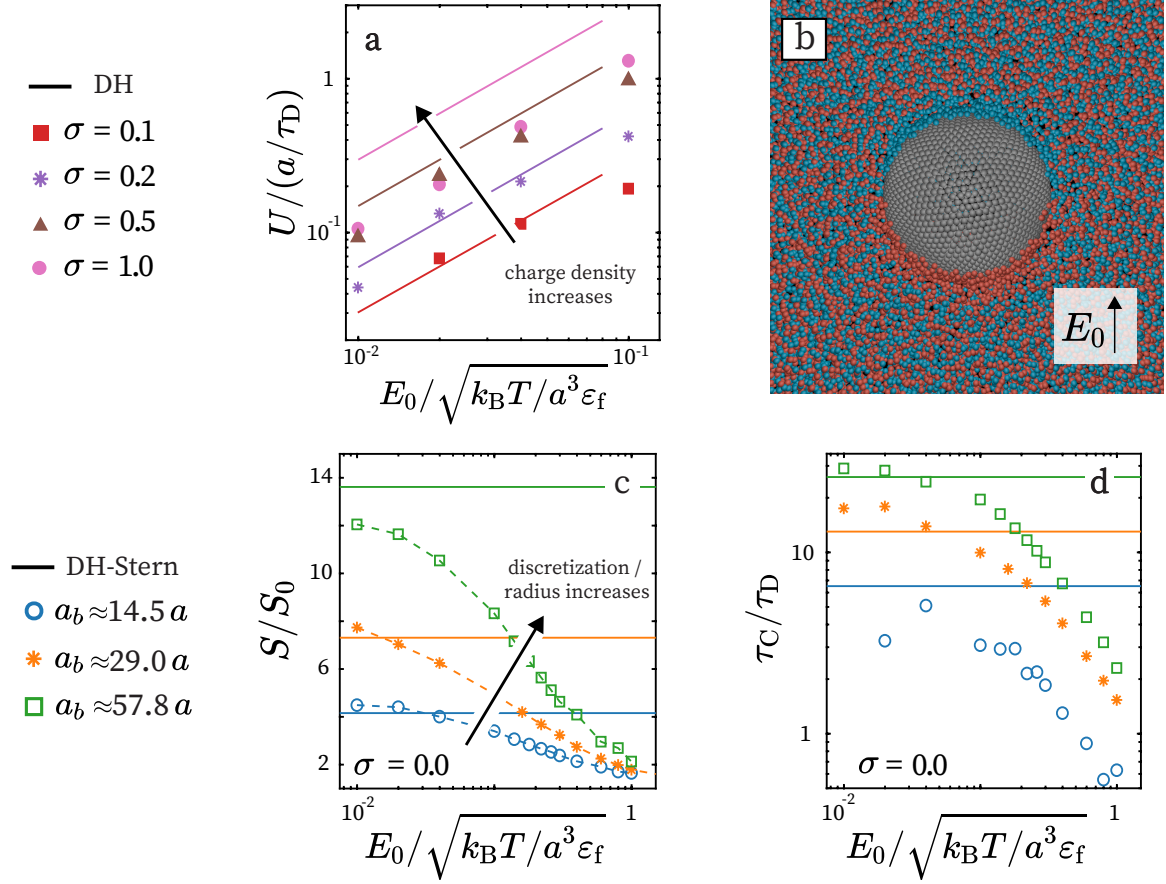


Figure 6. (a) Snapshot showing the induced charge and the resulting neutralizing double layer for an ideally polarizable body in an explicit electrolyte. The resulting double-layer structure is formed by electrosmotic effects due to the induced dipole moment of the ideally polarizable colloid. (b) Electrophoretic velocity as a function of the electric field. The results of charge densities $q_0 = 0.12$ (square markers), $q_0 = 0.24$ (starred markers), $q_0 = 0.62$ (triangle markers), and $q_0 = 1.22$ (circled markers), are shown in red, purple, brown, and pink, respectively. The solid lines correspond to the computed velocities in the thin double layer limit using eq. 50 (c) Evolution of the Body's induced dipole moment and (d) charging time of the electric double layer as a function of the externally applied field. The circled, starred, and squared markers correspond to discretization levels of $a_b = 15a$, $a_b = 30a$, and $a_b = 60a$ (comprising 42, 162, and 642 beads), respectively. Solid lines are obtained using the Debye-Hückel-Stern approximation.

wish to acknowledge the support from NASA, Grant No. 80NSSC18K0162 and NSF, Career Award No. 1554398.

i. Similarly, the summation tensor in eq. 15 is :

APPENDIX

Summation Tensors

The summation tensor, Σ , in eq. 13 is an $N_b \times N$ matrix whose rows correspond to rigid bodies and columns correspond to beads:

$$\Sigma \equiv \begin{bmatrix} \overbrace{1 \ 1 \ \dots}^{N_1} & \overbrace{0 \ 0 \ \dots}^{N_2} & \overbrace{0 \ 0 \ \dots}^{N_b} \\ 0 \ 0 \ \dots & 1 \ 1 \ \dots & 0 \ 0 \ \dots \\ 0 \ 0 \ \dots & 0 \ 0 \ \dots & 1 \ 1 \ \dots \\ \vdots & \vdots & \vdots \\ 0 \ 0 \ \dots & 0 \ 0 \ \dots & 1 \ 1 \ \dots \\ \vdots & \vdots & \vdots \end{bmatrix}, \quad (52)$$

Each row is entirely comprised by 0s, except for the N_i consecutive 1s corresponding to the N_i beads in the rigid body

$$\Sigma'' \equiv \begin{bmatrix} \overbrace{1 \ 1 \ \dots}^{N_1} & \overbrace{0 \ 0 \ \dots}^{N_2} & \overbrace{0 \ 0 \ \dots}^{N_b} \\ 0 \ 0 \ \dots & 1 \ 1 \ \dots & 0 \ 0 \ \dots \\ 0 \ 0 \ \dots & 0 \ 0 \ \dots & 1 \ 1 \ \dots \\ \vdots & \vdots & \vdots \\ \mathbf{r}_{11} \ \mathbf{r}_{12} \ \dots & 0 \ 0 \ \dots & 0 \ 0 \ \dots \\ 0 \ 0 \ \dots & \mathbf{r}_{21} \ \mathbf{r}_{22} \ \dots & 0 \ 0 \ \dots \\ 0 \ 0 \ \dots & 0 \ 0 \ \dots & \mathbf{r}_{31} \ \mathbf{r}_{32} \ \dots \\ \vdots & \vdots & \vdots \end{bmatrix}, \quad (53)$$

Force and torques derivation

The potential energy of the system is expressed as a sum of products of rigid body moments and potential derivatives⁴⁴

$$\begin{aligned} U &= \frac{1}{2} \sum_v (Q_v \Psi_i - \mathbf{S}_i \cdot \mathbf{E}_0) \\ &= \frac{1}{2} \mathbf{Q} \cdot \Psi_0 + \frac{1}{2} [\mathbf{q} \quad \Psi - \Psi_0] \cdot \begin{bmatrix} -\mathbf{r} \cdot \mathbf{E}_0 \\ \mathbf{Q} \end{bmatrix}. \end{aligned} \quad (54)$$

The induced charge distribution and rigid body potentials are computed from the inversion of equation (13),

$$\begin{aligned} U &= \frac{1}{2} \mathbf{Q} \cdot \Psi_0 \\ &+ \frac{1}{2} [-\mathbf{r} \cdot \mathbf{E}_0 \quad \mathbf{Q}] \cdot \begin{bmatrix} -\mathbf{M} & \Sigma^T \\ \Sigma & 0 \end{bmatrix}^{-1} \cdot \begin{bmatrix} -\mathbf{r} \cdot \mathbf{E}_0 \\ \mathbf{Q} \end{bmatrix}. \end{aligned} \quad (55)$$

The force on an individual bead α is the negative derivative of the potential energy with respect to the bead position \mathbf{x}_α , given

$$\begin{aligned} &- [-\mathbf{r} \cdot \mathbf{E}_0 \quad \mathbf{Q}] \cdot \left(\nabla_{\mathbf{x}_\alpha} \begin{bmatrix} -\mathbf{M} & \Sigma^T \\ \Sigma & 0 \end{bmatrix}^{-1} \right) \cdot \begin{bmatrix} -\mathbf{r} \cdot \mathbf{E}_0 \\ \mathbf{Q} \end{bmatrix} \\ &= [-\mathbf{r} \cdot \mathbf{E}_0 \quad \mathbf{Q}] \cdot \begin{bmatrix} -\mathbf{M} & \Sigma^T \\ \Sigma & 0 \end{bmatrix}^{-1} \cdot \begin{bmatrix} -\nabla_{\mathbf{x}_\alpha} \mathbf{M} & \nabla_{\mathbf{x}_\alpha} \Sigma^T \\ \nabla_{\mathbf{x}_\alpha} \Sigma & 0 \end{bmatrix} \cdot \begin{bmatrix} -\mathbf{M} & \Sigma^T \\ \Sigma & 0 \end{bmatrix}^{-1} \cdot \begin{bmatrix} -\mathbf{r} \cdot \mathbf{E}_0 \\ \mathbf{Q} \end{bmatrix} \\ &= [\mathbf{q} \quad \Psi - \Psi_0] \cdot \begin{bmatrix} -\nabla_{\mathbf{x}_\alpha} \mathbf{M} & 0 \\ 0 & 0 \end{bmatrix} \cdot \begin{bmatrix} \mathbf{q} \\ \Psi - \Psi_0 \end{bmatrix} \\ &= -\mathbf{q} \cdot \nabla_{\mathbf{x}_\alpha} \mathbf{M} \cdot \mathbf{q} \end{aligned} \quad (57)$$

Notice that because the summation tensor is constant, its gradient is zero, $\nabla_{\mathbf{x}_\alpha} \Sigma = 0$, and only the upper left block of the matrix survives. Thus, the force on bead α is

$$\mathbf{f}_\alpha = q_\alpha \mathbf{E}_0 - \frac{1}{2} (\nabla_{\mathbf{x}_\alpha} \mathbf{M}) : \mathbf{q} \mathbf{q} \quad (58)$$

Although the second term was written as $\mathbf{q} \cdot \nabla_{\mathbf{x}_\alpha} \mathbf{M} \cdot \mathbf{q}$ in (??), rewriting the equations in index notation shows that both dot products should contract the vector indices of the charges with the indices of the potential tensor, leaving the force with the same indices as the gradient. Therefore the proper vector notation is the double dot product in (58). The force and torque on a rigid body can then be computed from the distribution of bead forces,

$$\mathbf{F}_v = \sum_\mu \mathbf{f}_{v\mu}, \quad (59)$$

$$\mathbf{L}_v = \sum_\mu \mathbf{r}_{v\mu} \times \mathbf{f}_{v\mu}. \quad (60)$$

These forces and torques serve as the input to a rigid body hydrodynamic integrator that computes the rigid body velocities

all other beads remain fixed. Because the rigid body charges and external potentials do not depend on the bead positions, the negative derivative of the first term in (55), $-\nabla_{\mathbf{x}_\alpha} \mathbf{Q} \cdot \Psi_0/2$, vanishes. The product rule splits the negative derivative of the second term in (55) into three terms with the gradient acting only on one of the three matrices. The first of these terms is,

$$\begin{aligned} &- \left(\nabla_{\mathbf{x}_\alpha} [-\mathbf{r} \cdot \mathbf{E}_0 \quad \mathbf{Q}] \right) \cdot \begin{bmatrix} -\mathbf{M} & \Sigma^T \\ \Sigma & 0 \end{bmatrix}^{-1} \cdot \begin{bmatrix} -\mathbf{r} \cdot \mathbf{E}_0 \\ \mathbf{Q} \end{bmatrix} \\ &= [\nabla_{\mathbf{x}_\alpha} \mathbf{r} \cdot \mathbf{E}_0 \quad 0] \cdot \begin{bmatrix} \mathbf{q} \\ \Psi - \Psi_0 \end{bmatrix} \\ &= q_\alpha \mathbf{E}_0 \end{aligned} \quad (56)$$

and similarly for the term with the gradient applied to the third matrix. Notice that only the α^{th} component of $\nabla_{\mathbf{x}_\alpha} \mathbf{r} \equiv [\nabla_{\mathbf{x}_\alpha} \mathbf{r}_1, \nabla_{\mathbf{x}_\alpha} \mathbf{r}_2, \dots, \nabla_{\mathbf{x}_\alpha} \mathbf{r}_\alpha, \dots] = [0, 0, \dots, \mathbf{I}, \dots]$ is nonzero, so only the q_α term survives the dot product. The second term is,

and angular velocities of the composites by solving^{50,80}

$$\begin{bmatrix} \mathcal{M}^H & \Sigma'''^T \\ \Sigma''' & 0 \end{bmatrix} \cdot \begin{bmatrix} \mathbf{f}_c \\ \mathcal{U} \\ \Omega \end{bmatrix} = \begin{bmatrix} 0 \\ \mathcal{F} \\ \mathcal{L} \end{bmatrix} \quad (61)$$

where \mathbf{f}_c is a list of N constraint forces on each bead that hold the rigid composite together and Σ''' is a summation tensor defined in reference 50. $\mathcal{U} = [\mathbf{U}_1, \mathbf{U}_2, \dots, \mathbf{U}]^T$ is a list of rigid body velocities and similarly for the rigid body angular velocities Ω , rigid body forces \mathcal{F} , and rigid body torques \mathcal{L} . Each bead $v\mu$ then moves with a velocity specified by the translational \mathbf{U}_v and rotational Ω_v velocities of the rigid body v to which it belongs

$$\mathbf{u}_{v\mu} = \mathbf{U}_v + \Omega_v \times \mathbf{r}_{v\mu}. \quad (62)$$

REFERENCES

¹F. Caruso, ed., *Colloids and Colloid Assemblies: Synthesis, Modification, Organization and Utilization of Colloid Particles*, 1st ed. (Wiley, 2003).

- ²J. N. Israelachvili, *Intermolecular and surface forces*, 3rd ed. (Academic Press, Burlington, MA, 2011).
- ³D. Saville, W. Russel, and R. William, *Colloidal Dispersions*, Cambridge Monographs on Mechanics (1989).
- ⁴R. Kjellander and D. J. Mitchell, “Dressed ion theory for electric double layer structure and interactions; an exact analysis,” *Molecular Physics* **91**, 173–188 (1997).
- ⁵J. Ulander and R. Kjellander, “The decay of pair correlation functions in ionic fluids: A dressed ion theory analysis of monte carlo simulations,” *The Journal of Chemical Physics* **114**, 4893–4904 (2001).
- ⁶M. Z. Bazant and T. M. Squires, “Induced-Charge Electrokinetic Phenomena: Theory and Microfluidic Applications,” *Physical Review Letters* **92**, 066101 (2004).
- ⁷M. A. Gebbie, A. M. Smith, H. A. Dobbs, A. A. Lee, G. G. Warr, X. Banquy, M. Valtiner, M. W. Rutland, J. N. Israelachvili, S. Perkin, and et al., “Long range electrostatic forces in ionic liquids,” *Chemical Communications* **53**, 1214–1224 (2017).
- ⁸D. Ulberg, N. Churaev, V. Ilyin, and G. Malashenko, “Molecular dynamics simulation of the aggregation of colloidal particles,” *Colloids and Surfaces A: Physicochemical and Engineering Aspects* **80**, 93–102 (1993).
- ⁹E. Masoero, E. Del Gado, R. J.-M. Pellenq, S. Yip, and F.-J. Ulm, “Nanoscale mechanics of colloidal C–S–H gels,” *Soft Matter* **10**, 491–499 (2014).
- ¹⁰R. Chen, S. B. Kotkar, R. Poling-Skutvik, M. P. Howard, A. Nikoubashman, J. C. Conrad, and J. C. Palmer, “Nanoparticle dynamics in semidilute polymer solutions: Rings versus linear chains,” *Journal of Rheology* **65**, 745–755 (2021).
- ¹¹M. Eshraghi and J. Horbach, “Molecular dynamics simulation of charged colloids confined between hard walls: pre-melting and pre-freezing across the bcc–fluid coexistence,” *Soft Matter* **14**, 4141–4149 (2018).
- ¹²I. S. Sidhu, A. L. Frischknecht, and P. J. Atzberger, “Electrostatics of nanoparticle–wall interactions within nanochannels: Role of double-layer structure and ion–ion correlations,” *ACS Omega* **3**, 11340–11353 (2018).
- ¹³U. K. Padidela and R. N. Behera, “Interactions in charged colloidal suspensions: A molecular dynamics simulation study,” (2017), 10.1063/1.4990264.
- ¹⁴C. W. Outhwaite, S. Lamperski, and L. B. Bhuiyan, “Influence of electrode polarization on the capacitance of an electric double layer at and around zero surface charge,” *Molecular Physics* **109**, 21–26 (2011).
- ¹⁵Z. M. Sherman, D. Ghosh, and J. W. Swan, “Field-Directed Self-Assembly of Mutually Polarizable Nanoparticles,” *Langmuir* **34**, 7117–7134 (2018).
- ¹⁶K. Kang and J. K. G. Dhont, “Double-layer polarization induced transitions in suspensions of colloidal rods,” *EPL (Europhysics Letters)* **84**, 14005 (2008).
- ¹⁷J. Zhang, E. Luijten, and S. Granick, “Toward design rules of directional janus colloidal assembly,” *Annual review of physical chemistry* **66**, 581–600 (2015).
- ¹⁸S. W. Winslow, W. Shcherbakov-Wu, Y. Liu, W. A. Tisdale, and J. W. Swan, “Characterization of colloidal nanocrystal surface structure using small angle neutron scattering and efficient bayesian parameter estimation,” *The Journal of Chemical Physics* **150**, 244702 (2019), <https://doi.org/10.1063/1.5108904>.
- ¹⁹D. R. Ladiges, A. Nonaka, K. Klymko, G. C. Moore, J. B. Bell, S. P. Carney, A. L. Garcia, S. R. Natesh, and A. Donev, “Discrete ion stochastic continuum overdamped solvent algorithm for modeling electrolytes,” *Phys. Rev. Fluids* **6**, 044309 (2021).
- ²⁰J. F. Brady and G. Bossis, “Stokesian dynamics,” *Annual Review of Fluid Mechanics* **20**, 111–157 (1988).
- ²¹G. J. Elfring and J. F. Brady, “Active stokesian dynamics,” *Journal of Fluid Mechanics* **952**, A19 (2022).
- ²²J. W. Swan and G. Wang, “Rapid calculation of hydrodynamic and transport properties in concentrated solutions of colloidal particles and macromolecules,” *Physics of Fluids* **28**, 011902 (2016).
- ²³D. Zhang, P. González-Mozuelos, and M. Olvera de la Cruz, “Cluster formation by charged nanoparticles on a surface in aqueous solution,” *The Journal of Physical Chemistry C* **114**, 3754–3762 (2010), <https://doi.org/10.1021/jp9085238>.
- ²⁴J. Dobnikar, D. Haložan, M. Brumen, H.-H. von Grünberg, and R. Rzehak, “Poisson–Boltzmann Brownian dynamics of charged colloids in suspension,” *Computer Physics Communications* **159**, 73–92 (2004).
- ²⁵Z. Gan, H. Wu, K. Barros, Z. Xu, and E. Luijten, “Comparison of efficient techniques for the simulation of dielectric objects in electrolytes,” *Journal of Computational Physics* **291**, 317–333 (2015).
- ²⁶Z. Xu and W. Cai, “Fast Analytical Methods for Macroscopic Electrostatic Models in Biomolecular Simulations,” *SIAM Review* **53**, 683–720 (2011).
- ²⁷Z. Xu, W. Cai, and X. Cheng, “Image charge method for reaction fields in a hybrid ion-channel model,” *Communications in Computational Physics* **9**, 1056–1070 (2011).
- ²⁸A. Sangani and A. Acrivos, “The effective conductivity of a periodic array of spheres,” *Proceedings of The Royal Society A: Mathematical, Physical and Engineering Sciences* (1983), 10.1098/rspa.1983.0036.
- ²⁹A. Zangwill, *Modern electrodynamics* (2013).
- ³⁰K. F. Freed, “Perturbative many-body expansion for electrostatic energy and field for system of polarizable charged spherical ions in a dielectric medium,” *The Journal of Chemical Physics* **141**, 034115 (2014).
- ³¹Z. Gan, Z. Wang, S. Jiang, Z. Xu, and E. Luijten, “Efficient dynamic simulations of charged dielectric colloids through a novel hybrid method,” *The Journal of Chemical Physics* **151**, 024112 (2019).
- ³²K. Barros and E. Luijten, “Dielectric effects in the self-assembly of binary colloidal aggregates,” *Physical Review Letters* **113**, 017801 (2014).
- ³³X. Jiang, J. Li, X. Zhao, J. Qin, D. Karpeev, J. Hernandez-Ortiz, J. J. de Pablo, and O. Heinonen, “An $O(N)$ and parallel approach to integral problems by a kernel-independent fast multipole method: Application to polarization and magnetization of interacting particles,” *The Journal of Chemical Physics* **145**, 064307 (2016).
- ³⁴T. D. Nguyen, H. Li, D. Bagchi, F. J. Solis, and M. Olvera de la Cruz, “Incorporating surface polarization effects into large-scale coarse-grained Molecular Dynamics simulation,” *Computer Physics Communications* **241**, 80–91 (2019).
- ³⁵S. Tyagi, M. Süzen, M. Sega, M. Barbosa, S. S. Kantorovich, and C. Holm, “An iterative, fast, linear-scaling method for computing induced charges on arbitrary dielectric boundaries,” *The Journal of Chemical Physics* **132**, 154112 (2010).
- ³⁶M. Deserno and C. Holm, “How to mesh up Ewald sums. I. A theoretical and numerical comparison of various particle mesh routines,” *The Journal of Chemical Physics* **109**, 7678–7693 (1998).
- ³⁷A. Arnold, J. de Joannis, and C. Holm, “Electrostatics in periodic slab geometries. I,” *The Journal of Chemical Physics* **117**, 2496–2502 (2002).
- ³⁸M. Poursina and K. S. Anderson, “An improved fast multipole method for electrostatic potential calculations in a class of coarse-grained molecular simulations,” *Journal of Computational Physics* **270**, 613–633 (2014).
- ³⁹L. Greengard and V. Rokhlin, “A Fast Algorithm for Particle Simulations,” *Journal of Computational Physics* **135**, 280–292 (1997).
- ⁴⁰A. M. Fiore and J. W. Swan, “Fast stokesian dynamics,” *Journal of Fluid Mechanics* **878**, 544–597 (2019).
- ⁴¹M. Wang and J. F. Brady, “Spectral Ewald Acceleration of Stokesian Dynamics for polydisperse suspensions,” *Journal of Computational Physics* **306**, 443–477 (2016).
- ⁴²K. M. Reed and J. W. Swan, “The stress in a dispersion of mutually polarizable spheres,” *The Journal of Chemical Physics* **155**, 014903 (2021).
- ⁴³T. M. Squires and M. Z. Bazant, “Induced-charge electro-osmosis,” *Journal of Fluid Mechanics* **509**, 217–252 (2004).
- ⁴⁴J. D. Jackson, *Classical electrodynamics* (John Wiley & Sons, 1999).
- ⁴⁵L. D. Landau, L. E. M., P. L. P., J. B. Sykes, J. S. Bell, and M. J. Kearsley, *Electrodynamics of continuous media* (Pergamon Press, 1984).
- ⁴⁶R. T. Bonnecaze and J. F. Brady, “A method for determining the effective conductivity of dispersions of particles,” *Proceedings of The Royal Society A: Mathematical, Physical and Engineering Sciences* (1990), 10.1098/rspa.1990.0092.
- ⁴⁷Z. Sherman, *Self-Assembly and Dynamics of Colloidal Dispersions in Steady and Time-Varying External Fields*, Phd thesis, Massachusetts Institute of Technology (2019).
- ⁴⁸W.-F. Hu, M.-C. Lai, and Y.-N. Young, “A hybrid immersed boundary and immersed interface method for electrohydrodynamic simulations,” *Journal of Computational Physics* **282**, 47–61 (2015).
- ⁴⁹C. S. Peskin, “Flow patterns around heart valves: A numerical method,” *Journal of Computational Physics* **10**, 252–271 (1972).
- ⁵⁰J. W. Swan and G. Wang, “Rapid calculation of hydrodynamic and transport properties in concentrated solutions of colloidal particles and macromolecules,” *Phys. Fluids* **28**, 011902 (2016).
- ⁵¹K. Barros, D. Sinkovits, and E. Luijten, “Efficient and accu-

- rate simulation of dynamic dielectric objects,” *The Journal of Chemical Physics* **140**, 064903 (2014), https://pubs.aip.org/aip/jcp/article-pdf/doi/10.1063/1.4863451/14798154/064903_1_online.pdf.
- ⁵²D. Lindbo and A.-K. Tornberg, “Spectral accuracy in fast ewald-based methods for particle simulations,” *Journal of Computational Physics* **230**, 8744–8761 (2011).
- ⁵³J. Kolafa and J. W. Perram, “Cutoff errors in the ewald summation formulae for point charge systems,” *Molecular Simulation* **9**, 351–368 (1992).
- ⁵⁴M. P. Allen and D. J. Tildesley, *Computer Simulation of Liquids*, Vol. 1 (Oxford University Press, 2017).
- ⁵⁵A. M. Fiore and J. W. Swan, “Rapid sampling of stochastic displacements in brownian dynamics simulations with stresslet constraints,” *The Journal of Chemical Physics* **148**, 044114 (2018).
- ⁵⁶W. H. Press, ed., *Numerical recipes: the art of scientific computing*, 3rd ed. (Cambridge University Press, Cambridge, UK ; New York, 2007) oCLC: ocn123285342.
- ⁵⁷M. Wang and J. F. Brady, “Spectral ewald acceleration of stokesian dynamics for polydisperse suspensions,” *J. Comput. Phys.* **306**, 443–477 (2016).
- ⁵⁸D. Lindbo and A.-K. Tornberg, “Spectrally accurate fast summation for periodic stokes potentials,” *Journal of Computational Physics* **229**, 8994–9010 (2010).
- ⁵⁹Nvidia, “cufft,” developer.nvidia.com/cufft.
- ⁶⁰D. Ross, “The Potential Due to Two Point Charges Each at the Centre of a Spherical Cavity and Embedded in a Dielectric Medium,” *Australian Journal of Physics* **21**, 817 (1968).
- ⁶¹D. J. Jeffrey, “Conduction through a random suspension of spheres,” *Proceedings of The Royal Society A: Mathematical, Physical and Engineering Sciences* **335**, 355–367 (1973).
- ⁶²S. Torquato, *Random heterogeneous materials: microstructure and macroscopic properties*, Interdisciplinary applied mathematics No. 16 (Springer, New York, 2002).
- ⁶³D. Frenkel and B. Smit, *Understanding molecular simulation: from algorithms to applications* (Academic Press, 2002).
- ⁶⁴D. M. Heyes and P. J. Mitchell, “Self-diffusion and viscoelasticity of dense hard-sphere colloids,” *J. Chem. Soc., Faraday Trans.* **90**, 1931–1940 (1994).
- ⁶⁵D. Heyes and J. Melrose, “Brownian dynamics simulations of model hard-sphere suspensions,” *Journal of Non-Newtonian Fluid Mechanics* **46**, 1–28 (1993).
- ⁶⁶Z. Varga, G. Wang, and J. Swan, “The hydrodynamics of colloidal gelation,” *Soft Matter* **11**, 9009–9019 (2015).
- ⁶⁷J. Proakis and D. Manolakis, *Digital Signal Processing: Principles, Algorithms, and Applications*, Prentice-Hall International editions (Prentice Hall, 1996).
- ⁶⁸E. Krucker-Velasquez and J. W. Swan, “Underscreening and hidden ion structures in large scale simulations of concentrated electrolytes,” *The Journal of Chemical Physics* **155**, 134903 (2021), <https://doi.org/10.1063/5.0061230>.
- ⁶⁹B. Giera, N. Henson, E. M. Kober, M. S. Shell, and T. M. Squires, “Electric double-layer structure in primitive model electrolytes: Comparing molecular dynamics with local-density approximations,” *Langmuir*, **Langmuir** **31**, 3553–3562 (2015).
- ⁷⁰R. F. Stout and A. S. Khair, “Influence of ion sterics on diffusiophoresis and electrophoresis in concentrated electrolytes,” *Phys. Rev. Fluids* **2**, 014201 (2017).
- ⁷¹J.-P. Hansen and I. R. McDonald, *Theory of simple liquids* (Elsevier, 2006).
- ⁷²D. L. Goodstein, *States of matter*, unabridged and corrected republication ed., Dover Books in Physics (Dover Publications, Inc, Mineola, New York, 2014).
- ⁷³A. S. Khair and B. Balu, “The lift force on a charged sphere that translates and rotates in an electrolyte,” *Electrophoresis* (2019).
- ⁷⁴Z. M. Sherman and J. W. Swan, “Spontaneous Electrokinetic Magnus Effect,” *Physical Review Letters* **124**, 208002 (2020).
- ⁷⁵T. B. Jones, “Quincke Rotation of Spheres,” *IEEE Transactions on Industry Applications* **IA-20**, 845–849 (1984).
- ⁷⁶Y. Avni, R. M. Adar, D. Andelman, and H. Orland, “Conductivity of concentrated electrolytes,” *Phys. Rev. Lett.* **128**, 098002 (2022).
- ⁷⁷D. A. MacQuarrie, *Statistical mechanics* (University Science Books, 2000).
- ⁷⁸H.-B. Shi, G.-H. Gao, and Y.-X. Yu, “Self-diffusion coefficients of ions in primitive model electrolyte solutions by smart Brownian dynamics simulation,” *Fluid Phase Equilibria* **228-229**, 535–540 (2005).
- ⁷⁹J. A. Anderson, C. D. Lorenz, and A. Travasset, “General purpose molecular dynamics simulations fully implemented on graphics processing units,” *Journal of Computational Physics* **227**, 5342–5359 (2008).
- ⁸⁰G. Wang, A. M. Fiore, and J. W. Swan, “On the viscosity of adhesive hard sphere dispersions – critical scaling and the role of rigid contacts,” *J. Rheol.* **63**, 229–245 (2019).